Article

Mapping thalamic innervation to individual L2/3 pyramidal neurons and modeling their 'readout' of visual input

🔴 Check for updates

Aygul Balcioglu[1,2], Rebecca Gillani ◉[1,2,10], Michael Doron[3,4,11], Kendyll Burnell[1,2], Taeyun Ku ◉[1,5,6,12], Alev Erisir ◉[7], Kwanghun Chung ◉[1,4,5,8], Idan Segev[3,4] & Elly Nedivi ◉[1,2,9] ✉

The thalamus is the main gateway for sensory information from the periphery to the mammalian cerebral cortex. A major conundrum has been the discrepancy between the thalamus's central role as the primary feedforward projection system into the neocortex and the sparseness of thalamocortical synapses. Here we use new methods, combining genetic tools and scalable tissue expansion microscopy for whole-cell synaptic mapping, revealing the number, density and size of thalamic versus cortical excitatory synapses onto individual layer 2/3 (L2/3) pyramidal cells (PCs) of the mouse primary visual cortex. We find that thalamic inputs are not only sparse, but remarkably heterogeneous in number and density across individual dendrites and neurons. Most surprising, despite their sparseness, thalamic synapses onto L2/3 PCs are smaller than their cortical counterparts. Incorporating these findings into fine-scale, anatomically faithful biophysical models of L2/3 PCs reveals how individual neurons with sparse and weak thalamocortical synapses, embedded in small heterogeneous neuronal ensembles, may reliably 'read out' visually driven thalamic input.

The thalamus is the major hub of feedforward sensory information flow to the cerebral cortex, an important modulatory site for information en route from the periphery, and a critical component of cortical feedback loops[1,2]. How thalamic drive contributes to the firing properties of single cortical layer 4 (L4) neurons has been hotly debated[3–9], with scant attention paid to thalamic drive onto L2/3 PCs. Although the majority of thalamic inputs into neocortex synapse onto L4 and L1, there is also substantial thalamic innervation onto L2/3 neurons and their apical dendrites extending into L1 (refs. [10–12]). This direct thalamic drive onto neocortical L2/3 is becoming increasingly recognized as relevant to sensory processing[13,14], yet remains largely unexplored. In L4 of somatosensory cortex, the primary neocortical recipient layer for thalamic innervation, thalamocortical (TC) synapses account for 5–15% of synapses onto spiny neurons[15–19], with comparable density

[1]Picower Institute for Learning and Memory, Cambridge, MA, USA. [2]Department of Brain and Cognitive Sciences, Massachusetts Institute of Technology, Cambridge, MA, USA. [3]The Edmond and Lily Safra Center for Brain Sciences, Jerusalem, Israel. [4]Department of Neurobiology, The Hebrew University of Jerusalem, Jerusalem, Israel. [5]Institute for Medical Engineering and Science, Cambridge, MA, USA. [6]Department of Chemical Engineering, Massachusetts Institute of Technology, Cambridge, MA, USA. [7]Department of Psychology, University of Virginia, Charlottesville, VA, USA. [8]Broad Institute of Harvard University and MIT, Cambridge, MA, USA. [9]Department of Biology, Massachusetts Institute of Technology, Cambridge, MA, USA. [10]Present address: Department of Neurology, Massachusetts General Hospital, Boston, MA, USA. [11]Present address: Broad Institute of Harvard University and MIT, Cambridge, MA, USA. [12]Present address: Graduate School of Medical Science and Engineering, Korea Advanced Institute of Science and Technology, Daejeon, Republic of Korea. ✉e-mail: nedivi@mit.edu
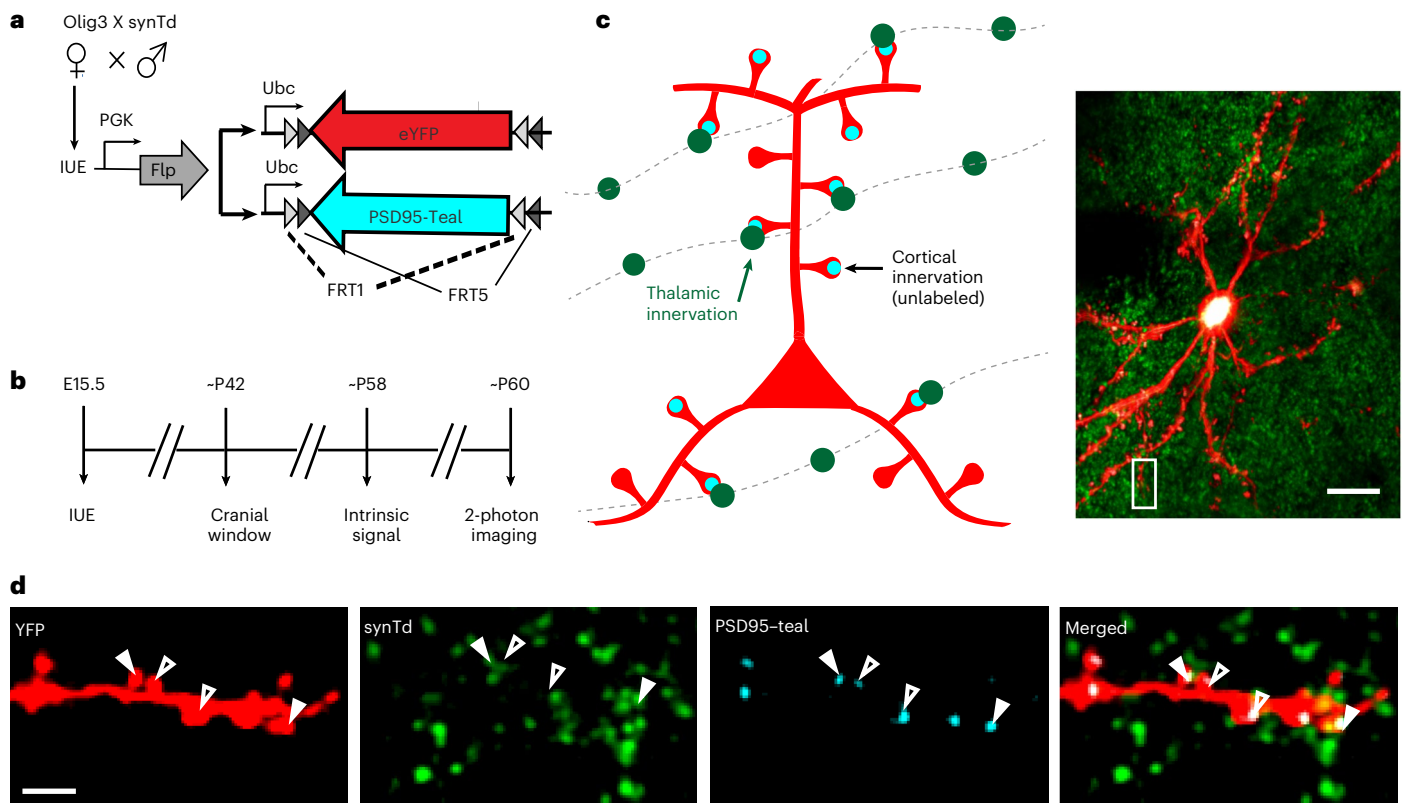
Fig. 1 | Specific labeling of thalamic excitatory afferents onto the full dendritic arbors of L2/3 pyramidal cells. a, Breeding strategy and plasmid combination for labeling of thalamic afferents onto an L2/3 postsynaptic target cell labeled with a cell fill and excitatory postsynaptic marker. Mice expressing Cre driven by the thalamus-specific Olig3 promoter were crossed to lox-stop-lox synTd mice (to label thalamic boutons). Pups were electroporated in utero at E15 with plasmids expressing Flp recombinase, flp-dependent eYFP (to label L2/3 PCs) and PSD95–Teal (to label excitatory synapses). **b**, Experimental timeline. Electroporated pups were raised to approximately 6 weeks of age, when a cranial window was placed above the visual cortex. Two weeks later, intrinsic signal optical imaging was used to map cell location to binocular visual cortex, followed within a few days by large-volume, high-resolution two-photon imaging of the entire cell dendritic arbor. **c**, Schematic representation of labeling outcome, with spines containing a PSD95 label overlapping a synTd bouton depicting thalamic inputs, and spines containing PSD95 without synTd overlap depicting intracortical excitatory inputs onto the same L2/3 pyramidal neuron. The inset shows a low-magnification maximum intensity *z*-projection of a two-photon imaging volume acquired in vivo of a neuron labeled with YFP cell fill (red) and PSD95-Teal (teal), with synTd (green) marking thalamic boutons. **d**, High-magnification views of the area boxed in the inset showing cell fill (red), thalamic boutons (green), PSD95 (blue) and overlay of all three color channels (merged). Filled white triangles mark spines where PSD95 overlaps with thalamic boutons, and empty triangles mark spines with putative intracortical synapses. Data shown in **c** inset and **d** are from one representative cell from nine experimental cells in nine different animals. Scale bars, 20 µm (top) and 5 µm (others).

in L2/3 (ref. [10]). In both L4 and L2/3, different neurons within the same lamina range in their response to thalamic drive[13]. Thus, both laminae pose similar enigmas in relation to how individual neurons with potentially sparse TC synapses, embedded in small heterogeneous ensembles, may reliably 'read out' sensory-driven thalamic input. This is further complicated by the fact that thalamic drive can originate from nuclei with different roles in sensory processing. In mice, the thalamic nuclei projecting to primary visual cortex (V1) are the lateral geniculate nucleus (LGN) and the lateral posterior (LP) complex.

Anatomical data that could be used to model thalamic drive onto individual neurons has thus far been lacking. Anatomical reconstructions by transmission electron microscopy (EM) have not yet generated whole-cell synaptic maps of TC versus corticocortical (CC) inputs across multiple cells. Even with modern large-scale connectomics, unless an axon can be directly traced to a nearby 'source' neuron, its origin cannot be definitively identified. Thalamic (and most cortical) afferents fall well outside the reconstructed volume of even the most comprehensive image stacks available to date. EM combined with track tracing or immunostaining allows characterization of distinct inputs to a particular layer, but is limited due to sampling and measurement biases on two-dimensional cross-sections[20]. Furthermore,

two-dimensional EM cannot provide a map of all thalamic inputs onto a given cortical neuron, and efforts to combine EM with genetic labels that can classify cell and synapse type have not yet been successful. To date, there has been no anatomical characterization of where thalamic inputs map onto the dendritic arbors of individual cortical pyramidal neurons, or distinction of which thalamic nuclei give rise to these projections.

Here we apply genetic and molecular labeling strategies to identify the complement of TC inputs onto 15 L2/3 PCs imaged in vivo in mouse V1, and show that they derive from the LGN. Six of these cells were processed using post hoc magnified analysis of proteome (MAP), a newly developed tissue transformation method that enables super-resolution proteomic imaging of large-scale tissues[21,22], allowing proteomic validation of thalamic versus cortical synapses and measurement of their respective sizes, and relative numbers. Our findings suggest that TC synapses onto L2/3 PCs are both sparse and small, and their number and distribution are quite heterogeneous between individual dendritic branches and cells. We incorporate this novel fine-scale anatomical information into a detailed biophysical model of L2/3 PCs from V1, demonstrating how such sparse and relatively weak feedforward TC drive can generate visual responses in L2/3 PCs, and how a relatively
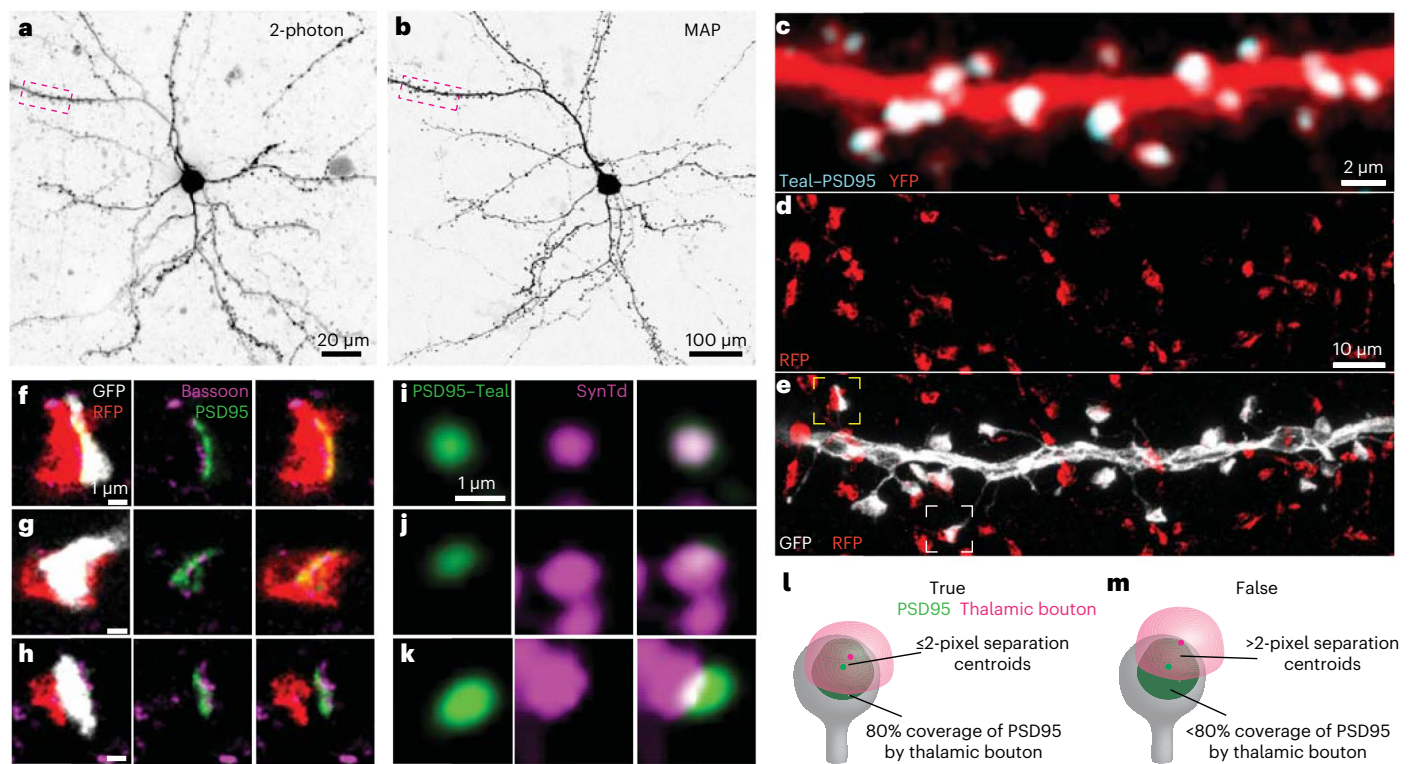
Fig. 2 | Magnified analysis of the proteome allows validation of two-photon scoring criteria for true thalamic boutons. a,b, Maximum intensity z-projections of a cell with YFP fill imaged in vivo with two-photon microscopy (**a**), and post hoc after MAP with an anti-GFP label (**b**). Scale bars, 20 μm (**a**) and 100 μm (**b**). **c–e**, Maximum intensity z-projections of dendritic segment boxed in **a** and **b**. **c**, Two-photon image showing YFP cell fill (red) and PSD95 label (teal). Scale bar, 2 μm. **d,e**, Same segment in MAP-processed brain labeled with anti-GFP to visualize cell fill (white), and anti-RFP (red) to label genetically encoded tdTomato in thalamic boutons. **a–e**, n = 3 cells from three animals.

Scale bar, 10 μm. **f,g**, Magnified view of one x–y plane for the yellow (**f**) and white (**g**) boxed thalamic innervated spines in **e**, labeled with anti-Bassoon (magenta) and anti-PSD95 (green). Note the perfect apposition of Bassoon and PSD95, and their full overlay with both RFP and GFP. n = 49 LGN synapses from three animals. **h**, Magnified view of cortical innervated spine (not pictured in **e**), Bassoon and PSD95 do not overlap RFP. n = 834 cortical synapses from three animals. **i–k**, One x–y plane from two-photon image of spines in **f–h**. Scale bars in **f–k**, 1 μm. **l,m**, Schematic illustrating two-photon scoring criteria for thalamic (**l**) versus cortical (**m**) synapses.

small L2/3 PC assembly can reliably interpret ('read out') visual drive relayed through thalamus.

Results

Labeling thalamic inputs onto single L2/3 pyramidal cells

To visualize thalamic synapses onto L2/3 PCs of V1, we used a strategy for sparse triple-color neuronal labeling similar to one we recently developed[23,24]. PCs were labeled with two fluorophores—eYFP to visualize cell morphology, including dendritic spines, and postsynaptic density protein 95 fused to teal fluorescent protein (PSD95–Teal) to mark mature excitatory synapses—with the third fluorophore labeling thalamic inputs. Thalamic boutons were labeled by crossing transgenic mice harboring lox-stop-lox synaptophysin-tdtomato (synTd) with mice expressing Cre under the control of the Olig3 promoter (Fig. 1a–d). Crossing the Olig3-Cre driver line with the Ai14 reporter line showed labeling in LGN, but not LP, indicating the Olig3 line expression in thalamic visual nuclei is specific to LGN (Extended Data Fig. 1a–j).

Pups from the Olig3$^{+/-}$;synTd$^{+/+}$ cross were electroporated at embryonic day (E) 15.5, to target L2/3 PCs in V1 with a combination of three plasmids: Flp-dependent eYFP and Flp-dependent PSD95–Teal plasmids at high concentration, and a Flp recombinase plasmid in limiting amounts, to achieve high incidence of fluorophore coexpression together with sparse labeling. When pups reached adulthood, labeled neurons were selected in binocular V1 and imaged through a cranial window at diffraction-limited resolution using a custom-built two-photon microscope[24] (Fig. 1d and Extended Data Fig. 2). We were thus able to visualize spines and excitatory synapses across entire L2/3

PCs, and identify which synapses were receiving LGN input. Spine and excitatory synapse densities were comparable with this new labeling constellation to prior studies using Cre-dependent postsynaptic fluorophore expression (Extended Data Fig. 3a).

Super-resolution discrimination of LGN versus cortical synapses

To establish criteria for scoring LGN synapses imaged in vivo, we used MAP[21,22], a method that clears and isotropically expands tissue with preservation of its three-dimensional (3D) architecture while maintaining the relationships between subcellular structures, also allowing the labeling of endogenous proteins with standard commercially available antibodies. Three L2/3 PCs labeled for cell fill, PSD95 and thalamic boutons, as described above (Fig. 1), were processed for MAP immediately after in vivo imaging (Fig. 2a,b), followed by immunostaining for GFP to visualize cell fill, RFP and/or VGlut2 to label thalamic presynaptic terminals, PSD95 and Bassoon (Fig. 2c,e). A total of 49 synapses were identified as LGN innervated in MAP images based on apposition of a synTd/RFP bouton with a dendritic spine head, where PSD95 and/or Bassoon were used to confirm location of the physical synapse (Fig. 2f,g).

We then examined the two-photon images corresponding to the 49 LGN synapses validated by MAP, as well as 834 non-LGN synapses (Fig. 2f–k). We found that two-photon images of LGN synapses confirmed by MAP showed at least 80% 3D coverage of the PSD95 fluorescence signal by synTd, with no more than a two-pixel separation of PSD95 and synTd centroids in xy, and no more than one z-step of separation (Fig. 2l,m). Blind scoring of the two-photon data using
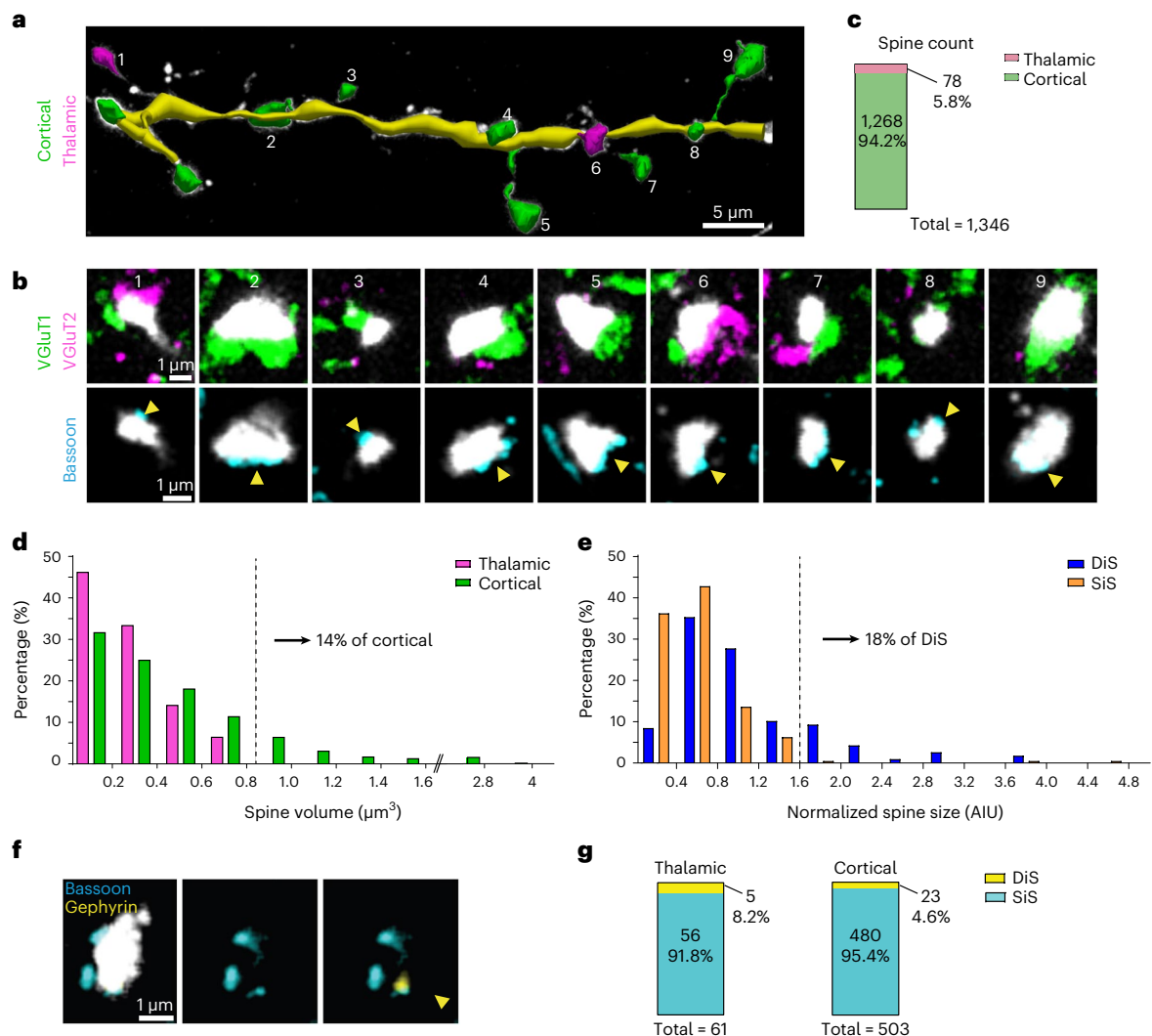
Fig. 3 | Every PSD95⁺ spine receives either thalamic or cortical input, with thalamic inputs favoring smaller spines. Inhibitory synapses target spines receiving either thalamic or cortical input. a, Maximum intensity z-projection of a MAP-imaged dendritic segment with Neurolucida 360 3D reconstruction and morphometric spine modeling. Reconstructed dendritic segment shown in yellow overlaid on anti-GFP stain (white), with every PSD95⁺ spine identified as thalamic (magenta) or cortical (green) based on MAP images. Scale bar, 5 μm. **b**, Magnification of one x–y plane from numbered spines in **a**, shown in white. Top part shows round 1 of immunostaining for VGluT1 (cortical, green) and VGlut2 (thalamic, magenta). Bottom part shows round 2 immunostaining for Bassoon (cyan), marking synaptic location for each spine/bouton junction. Spine 9 has a synapse projecting in the z-dimension. Scale bar, 1 μm. **c**, Proportion of thalamic and cortical spines among 1,346 analyzed spines (432 apical; 914 basal) from five different MAP processed neurons, each from a different animal. **d**, Relative frequency distribution of thalamic and cortical dendritic spine volumes for 799 modeled spines from five different neurons, each from a different animal.

Dendritic spines containing thalamic synapses were significantly smaller than dendritic spines containing cortical synapses (two-way analysis of variance (ANOVA), $F(1,789) = 24.70, P < 0.0001$). Of the cortical spine population, 14% are larger than the largest thalamic spines. **e**, Adapted from ref. [24]; AIU, average intensity units. Relative frequency distribution of SiSs containing only PSD95, and DiSs containing both PSD95 and Gephyrin. Of DiSs, 18% are larger than the largest SiS, with very few exceptions. The largest population of dendritic spines are exclusively cortical in MAP images, and exclusively DiSs in two-photon images. Note that the distribution of spine size measurements is compatible between MAP and two-photon images. **f**, One x–y plane of a dendritic spine receiving cortical input (Vglut2 negative), shown in white, with an inhibitory synapse stained with Bassoon (cyan) and Gephyrin (inhibitory synapse, yellow). $n = 28$ inhibitory synapses from one animal. **g**, Proportion of spines receiving thalamic or cortical input that contain an inhibitory synapse. $n = 61$ thalamic spines and 503 cortical spines from one animal.

these criteria found a close match between the two-photon and MAP data, with a false positive rate of 0.6% (0.4% for cell 1, 0.9% for cell 2 and 0.4% for cell 3), and a false negative rate of 18% (four synapses for cell 1, three for cell 2 and two for cell 3). Attempts to relax scoring criteria to decrease the false negative rate resulted in an increase in false positives.

Three additional L2/3 PCs labeled for cell fill and PSD95, but not synTd, were imaged and processed for MAP, then immunostained for VGlut1 and VGlut2 to label cortical and thalamic presynaptic terminals, respectively, in addition to GFP to visualize cell fill, PSD95 and Bassoon

(Fig. 3a,b). We found that every PSD95-positive dendritic spine was contacted by either a VGlut2 or a VGlut1 positive input, but never both. SynTd boutons all stained positive for VGlut2 (Extended Data Fig. 1k–q), further confirming LGN origin of the Olig3/synTd-labeled afferents. In contrast to the LGN that sends VGlut2-positive projections to V1, LP's projections to V1 are VGlut2 negative and go preferentially to L1 and supragranular layers L5 and L6, while VGlut2-expressing LP neurons project to extrastriate areas[25–27]. The lack of LP projections to superficial layers of V1 and the 1:1 synTd-VGlut2 match allowed us to designate any

PSD95-positive spine that was VGlut2 negative as cortical. Overall, we scored 1,346 LGN and cortical synapses across five MAP-processed cells (Figs. 3c)—two with synTd labeling of LGN boutons, and three without. This represents a substantial sample size as compared to other super-resolution methods, as well as EM.

LGN synapses are smaller than their cortical counterparts

Prior observations had predicted that thalamic synapses would be stronger than their cortical counterparts[28–30]. Further, we have previously reported that dually innervated spines (DiSs) containing both PSD95 and Gephyrin tend to be larger than singly innervated spines (SiSs) containing only PSD95 (ref. [24]), and it has been suggested that these DiSs are thalamically innervated[28], consistent with the expectation that thalamic synapses are large. To examine whether this is indeed the case, we performed morphometric size modeling of 799 dendritic spines from the 5 different MAP neurons (Fig. 3d). Surprisingly, we found that dendritic spines containing LGN synapses were significantly smaller than dendritic spines containing cortical synapses (Fig. 3d; $F(1, 789) = 24.70$, $P < 0.0001$; least-squares mean thalamic = 0.27 µm³, least-squares mean cortical = 0.49 µm³, standard error of the difference between means = 0.04). The largest dendritic spines were mostly cortical. This finding could not be attributed to any technical artifact of synTd labeling or the MAP method (Extended Data Figs. 3b and 4). Our prior data show that the largest dendritic spines are almost exclusively DiSs (Fig. 3e), implying that the largest dually innervated dendritic spines are more likely to harbor cortical synapses. To examine this directly, three additional cells labeled as described (Methods), were processed for MAP and stained for eYFP, Bassoon, VGlut2 and gephyrin to identify DiSs receiving thalamic input. While the proportion of thalamic versus cortical synapses onto DiSs was higher (8.2% versus 4.6%), because cortical synapses are almost ten times more abundant, the likelihood of the excitatory synapse on a DiS being cortical versus thalamic was almost 5:1 (Fig. 3f,g). Thus, prior assumptions that excitatory innervation of DiSs is mostly thalamic are incorrect.

Heterogeneous LGN innervation between and across neurons

Another surprise from the MAP analysis, was the heterogeneity in LGN innervation between neurons (2%, 6%, 8%, 9% and 10% thalamic of all scored synapses on five MAP-processed cells). To further investigate thalamic synapse density and distribution across a larger neuronal population, we analyzed nine additional neurons labeled as described in Fig. 1 and imaged in vivo in their entirety. Based on the MAP-defined scoring criteria, we were able to designate every excitatory input onto these neurons as either LGN (PSD95 label overlaps with a synTd bouton) or cortical (PSD95 label does not overlap with a synTd bouton). Overall, across all nine cells, the mean synaptic densities were 0.2 ± 0.064 synapses/micron, for CC synapses and 0.038 ± 0.012 synapses/micron, for TC synapses. The coefficients of variance for these synapses were 0.31 and 0.33 synapses/micron, respectively. Similarly to our MAP findings, we saw surprising heterogeneity in the distribution and density of thalamic innervation to L2/3 PCs only imaged in vivo (Fig. 4a,b and Extended Data Fig. 5), with no obvious correlation to cell depth or morphology (Fig. 4a,b and Extended Data Figs. 5 and 6). Tremendous

heterogeneity in synaptic density was also evident between individual branches of the same neuron (Extended Data Fig. 7). Some branches had 0 thalamic synapses (for example, branch 11 of both cell 1 and 2, branch 17 of cell 7), while others had as many as 33 TC synapses, or 45% thalamic input of the total excitatory synapses to these branches (for example, branch 8 of cell 1 and branch 11 of cell 6, respectively).

LGN synapse distribution is not random

Aside from their heterogeneous distribution across neurons, when computing the ratio of TC/CC synapses on the basal versus the apical tree for all nine L2/3 cells imaged in vivo, we found that the TC/CC ratio was larger in the basal tree of all cells, with an average ratio of 0.2 on basal dendrites and 0.12 on apical dendrites ($P = 0.0445$; Fig. 4c–e). This was not due to higher local bouton densities near basal branches, as dendritic targeting by LGN synapses was uncorrelated with either branch depth nor local bouton density (Extended Data Fig. 8).

We next asked whether TC or CC synapses were randomly distributed along dendrites. We calculated the distance between each synapse type to its nearest neighbor and compared it to the respective random distribution (Methods). We found that both CC and TC synapses tended to be closer to each other than expected in the random case, with average nearest-neighbor distance of 9.55 µm for TC synapses as compared to 13.25 ± 1.07 µm in the respective random case ($P < 0.0001$; Fig. 4f), and 2.34 µm for CC synapses compared to 2.48 ± 0.05 µm in the respective random case ($P < 0.0001$; Fig. 4g). This means that both TC and CC synapses are more clustered among themselves than expected from a random distribution. In contrast, the distance between TC synapses and their closest CC counterpart was larger than expected in the respective random case (Fig. 4h). Whereas the average distance between TC-to-CC synapses was 2.57 µm, the distance in the respective random case was 2.41 µm ± 0.14 µm ($P < 0.0001$). Thus, both thalamic and cortical synapses show a marked preference for 'like' neighbors and tend to avoid each other. We saw no difference in the average distance of TC versus CC synapses from the soma (92 µm ± 0.28 for TC, and 94 µm ± 0.22 for CC).

Effect of thalamic input heterogeneity on L2/3 pyramidal cell responses

To explore the computational implications of heterogeneity in number and density of thalamic synapses on the firing properties of L2/3 PCs in mouse V1, we first constructed a detailed biophysical model for a prototypical L2/3 PC from mouse V1 that faithfully matched the passive and active properties of these cells, as well as the expected, experimentally based, peak conductance (~0.3 nS) of individual TC synaptic contacts (Extended Data Fig. 9 and Methods). We next mapped the experimentally determined synaptic densities (per cell) onto the biophysical cell model and activated the TC synapses, as well as 12% of the CC synapses (representing L4-to-L2/3 synapses) with a simulated drifting sinusoidal visual input (Methods and ref. [31]). In Fig. 5a–c, three modeled cells (cells 3, 5 and 6) are shown, receiving a 1-s-long drifting sinusoidal grating input at 1 Hz and 100% contrast. The density of TC and CC synapses is shown in the respective insets, whereas the raster plot of the cell's output spike is shown in the middle in each case. Cell 3 did not generate output spikes in response to the visual input with
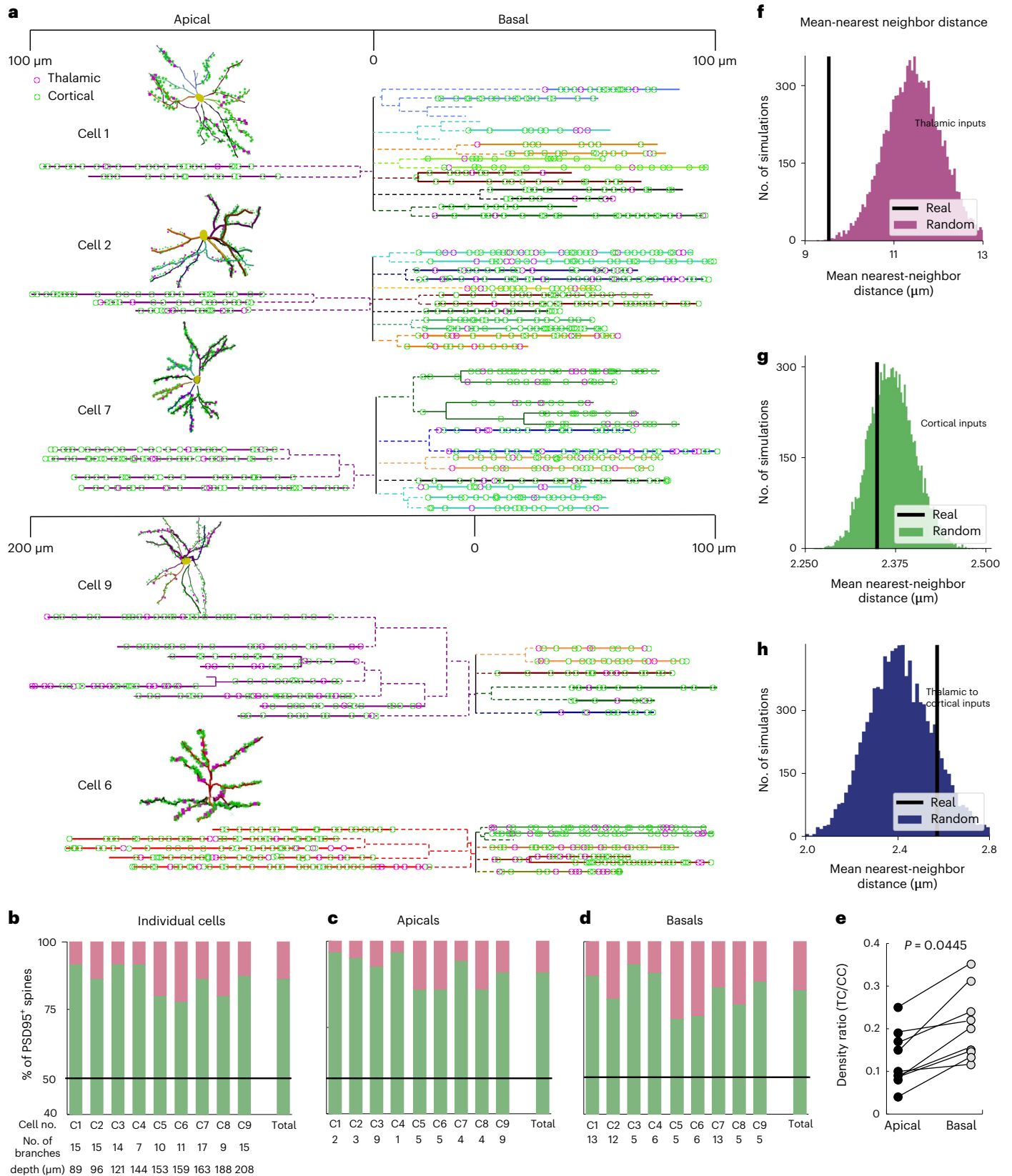
Fig. 4 | Distribution of thalamic versus cortical synapses onto L2/3 neurons. a, Representative dendrograms showing the distribution of thalamic versus cortical synapses onto the dendritic arbors of five different pyramidal neurons in L2/3 of binocular V1. Apical and basal dendrites are shown on opposite sides of the cell body (marked as 0 on the scale). The scale illustrates the distance of each synapse from the cell body. Cells 9 and 6 are deeper, with longer apical dendrites, and are thus shown on a different scale. Dashed lines depict branch segments that were traced, but not scored. Insets (top left) in each dendrogram show the traced skeleton of that cell with location of scored synapses. Note the uneven distribution of thalamic and cortical synapses across different cells and individual dendritic branches. **b**, Variance in thalamic synapse distribution across different cells. **c**, Variance in thalamic synapse distribution across the apical dendrites of different cells. **d**, Variance in thalamic synapse distribution across the basal dendrites of different cells. **e**, The ratio of TC/CC synaptic density in apical versus basal dendrites, showing that TC synapses significantly favored basal as compared to apical dendrites ($P = 0.0445$, two-sided t-test). **f**, Actual mean distance between TC synapse to its nearest neighbor (black vertical line) and the respective random case (magenta histogram). x axis is the mean nearest-neighbor distance in millimeters, y axis is the number instances in which a particular average distance was obtained. **g**, As in **f**, for CC synapses. **h**, As in **f**, showing the distance between each TC synapse to its nearest CC synapse neighbor.

low frequency; cell 5 responded with multiple spikes, whereas cell 6 fired intensely during the positive phase of the sinusoidal visual input. Note that cell 6 had less TC synapses than cell 5 but it had more CC excitatory synapses (and thus stronger background synaptic activity; Methods). The middle and lower rows in Fig. 5 show the response of the same three modeled cells to visual input fluctuating at 4 Hz with 100%

contrast (Fig. 5d–f) and 50% contrast (Fig. 5g–i). The large variability among cells' output in response to identical visual input is apparent throughout a range of visual input parameters. Our modeling therefore predicts that the anatomical variability in synaptic density onto different L2/3 PCs would manifest in a large variability in their firing response to visual input.
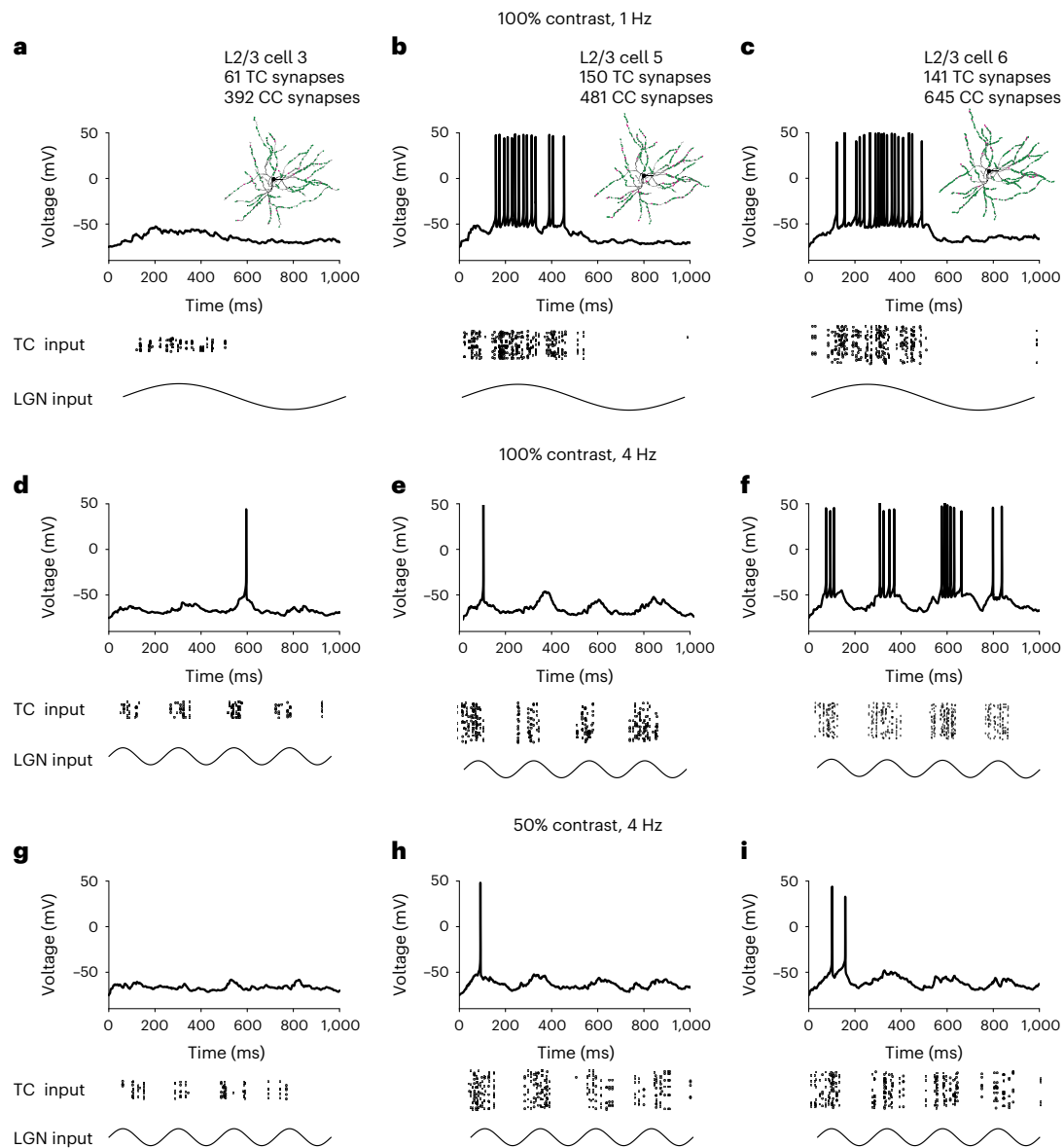

Fig. a Apical / Basal morphological reconstructions showing Thalamic and Cortical synapses for Cell 1, Cell 2, Cell 7, Cell 9, Cell 6.

f Mean-nearest neighbor distance — Thalamic inputs. Real vs Random.

g Cortical inputs. Real vs Random.

h Thalamic to cortical inputs. Real vs Random.

b Individual cells — % of PSD95⁺ spines.

c Apicals.

d Basals.

e Density ratio (TC/CC), P = 0.0445, Apical vs Basal.

Cell no.	C1	C2	C3	C4	C5	C6	C7	C8	C9
No. of branches	15	15	14	7	10	11	17	9	15
depth (µm)	89	96	121	144	153	159	163	188	208

Fig. 5 | Thalamocortical and corticocortical synaptic variability results in large response variability of L2/3 cells to visual input. a, Top, voltage response of the L2/3 PC model to a moving grating visual input at 1 Hz and 100% contrast, with the TC and CC synaptic densities taken from the imaged cell 3 (Methods). Inset shows the modeled cell and its respective number of TC and CC synapses, with the locations of the CC (green) and TC synapses (magenta). Middle, raster plot showing the (modulated) activation time of TC synapses in the model, in response to the visual input (bottom). 12% of the CC synapses, representing excitatory input from L4, were activated by a simulated drifting sinusoidal visual input, with a 5-ms delay with respect to the modulated TC synapses. The activation times of the rest of the CC synapses and the inhibitory synapses were sampled from a Poisson distribution (Methods). **b,c**, Same as in **a**, with synaptic distribution taken from cells 5 and 6, respectively. **d–f**, as in **a–c**, but with visual input at 4 Hz. **g–i**, same as in **d–f**, with 50% visual contrast.

The large variability in cells' outputs for a given visual input (also reported in vivo[32]) raises the issue of visual input readout quality[33–36]. To address this, we examined to what degree a simple linear decoder, receiving the output firing rate of the modeled cells as an input, could estimate the contrast of the respective visual input. In Fig. 6a we show that, for an input frequency of 4 Hz, the linear decoder from each individual cell provides a poor prediction of the visual input contrast (R^2 ranges between 0.08 and 0.52 among the nine modeled cells, with an average of 0.34). However, when the decoder was provided with the firing rates of the nine modeled cells simultaneously, the decoding accuracy was much improved ($R^2 = 0.79$). When extrapolating our results based on the readout accuracy using 1, 2, ... 9 cells, our model predicted that using the firing rates of 12 L2/3 cells, the decoder predicted the input contrast at an accuracy of 90%.

To explore which of the variable parameters of the L2/3 PCs impacted this readout accuracy, we examined the relationship between the readout accuracy of a given cell model and the average firing rate of that cell (Fig. 6b), as well as the relationship between the readout accuracy of the cell and the total number of TC plus CC synapses it received (Fig. 6c). Figure 6b shows a steep correlation between cell firing frequency in response to the visual input and the readout accuracy, which flattens out when the firing frequency of the cell grew to 4–5 Hz. Figure 6c shows that, for the range of parameters used in this study, readout accuracy increased rather linearly with the number of synapses per modeled cell. In Fig. 6d, we examined the readout accuracy as a function of the total number of both TC and the CC synapses over all cells used for the readout, in both the heterogeneous case, where the readout was based
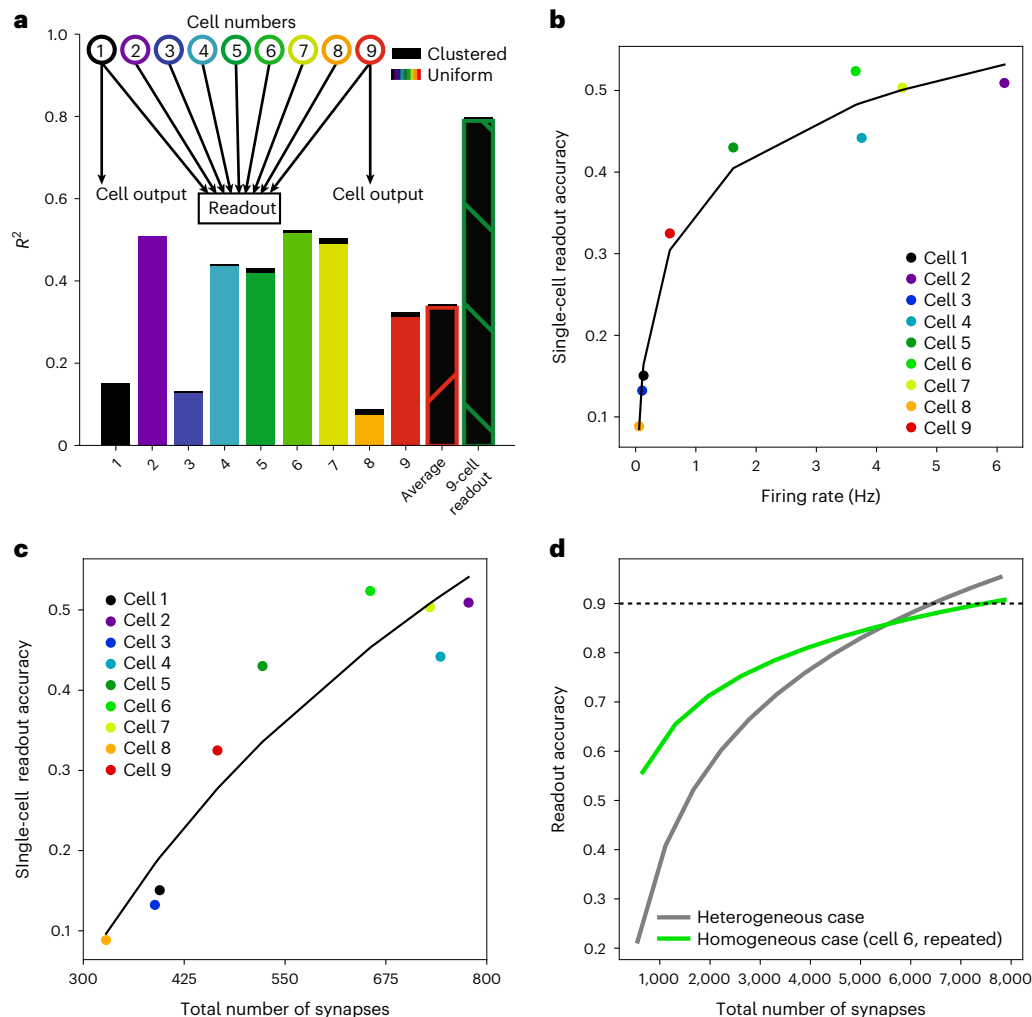
Fig. 6 | Heterogenous synaptic density among L2/3 cells improves readout accuracy of visually driven thalamic input. a, Inset, schematics for the readout models; upper row shows models for cells 1 to 9, each using the same prototypical cell model but with respective TC and CC synaptic densities taken from our nine experimental cells. The output firing rate of these cells' models were used as the input to a linear 'readout cell'. In one case, the firing rate of an individual modeled cell was used for the readout, whereas in the second case the linear readout utilized the firing rates of all nine cells combined (Methods). Bars show the accuracy of linear regression model (in units of squared Pearson correlation, R^2) in predicting the visual contrast at a frequency of 4 Hz; it was low when based on an individual cell's output but increased substantially when based on the combined output of all nine cells. Color bars show the readout quality when the synapses were randomly distributed over the dendritic surface; the thin black bar at top shows the case whereby both the TC and the CC synapses were spatially clustered as found experimentally. **b**, Relationship between the readout accuracy of a given cell model and the average firing rate of this cell for a 4-Hz visual input at maximal contrast. **c**, Relationship between the readout accuracy of a given cell model and the total number of TC plus CC synapses in this cell for a 4-Hz visual input at maximal contrasts. **d**, Extrapolation of the readout accuracy as a function of the total number of both TC and the CC synapses, summed over all cells used for the readout. We trained a linear regressor to predict the input parameters based on the individual cells' output. The curve shows the extrapolation of the accuracy of the linear regressor as a function of the total number of synapses across all cells (Methods). Based on the results for the 9-cell readout, we extrapolated that 12 cells would be required to reach 90% accuracy in the heterogeneous case. In the homogeneous case, the outputs of the best performing cell (cell 6), repeated multiple times was used to train the linear regressor (Methods). Note the 'saving' of synapses in the heterogenous case when aiming at high readout accuracy (for example, for 90% readout accuracy, 6,673 synapses were required in the heterogenous case and 7,866 synapses were required in the homogenous case; Methods).

on the (variable) output of our nine modeled cells, and the homogeneous case, whereby the readout quality was based on the outputs of the best performing cell (cell 6) repeated multiple times (Methods). Interestingly, we found that a larger number of TC + CC synapses was required in the homogeneous as compared to the heterogeneous case to achieve high readout accuracy. For example, for a 90% readout accuracy, 6,673 synapses were required in the heterogeneous case, while 7,866 synapses were required in the homogenous case. Thus, heterogeneity imparts a 'cost' reduction in terms of the number of synapses required for accurate readout of visual features (Discussion).

Discussion

A substantial barrier to understanding the role of thalamus in cortical function is our limited knowledge regarding the basic connectivity between these two crucial and complex brain structures[2]. Previous studies, mostly focused on thalamic projections to L4, advanced our understanding of how the thalamus contributes to visual processing in the neocortex. Yet, lacking the detailed anatomical mapping of thalamic input size and location onto individual cortical neurons, the studies could not address the question: 'what is the relative contribution of thalamic versus cortical synapses to the activity of a single visually responsive

cortical neuron, and how would this support readout of a visual stimulus by visual cortex?'

By combining genetic and molecular labeling technologies with in vivo multispectral two-photon microscopy, we were able to image the complement of excitatory synapses onto individual L2/3 PCs as well as afferent inputs from the main thalamic nucleus projecting to L2/3 of V1–the LGN. Subsequent MAP analysis with a newly developed method for tissue expansion and clearing provided 3D super-resolution imaging of the same cells, so that we could designate each excitatory synapse as either from LGN or from cortex, and measure their dendritic location and respective sizes. Thus, we generated a precise synaptic/dendritic dataset ('synaptic map') that could be incorporated for the first time into detailed models, realistically bound by anatomical data, of cortical L2/3 PCs responding to thalamic drive from the LGN. L2/3 cells receive substantial thalamic input, second only to L4 cells[10,13]. L2/3 pyramidal neurons amplify the sensory-evoked inputs from thalamus directly onto L5 neurons, providing gain control for the thalamic drive onto these neurons[14]. Importantly, with evolution, the thickness of L2/3 becomes increasingly more prominent, and is much expanded in primates and humans, as compared to rodents[37]. This warrants future examination of thalamic inputs to L2/3 in these species, and how they may contribute to cortical readout of thalamic signals.

Anatomically precise mapping of LGN inputs onto L2/3 PCs revealed several unexpected features. The first is the remarkable heterogeneity of input number and distribution across individual dendrites, and different neurons. The second, is the seemingly conflicting findings that LGN synapses onto these cells are both sparse and small. While prior models have mostly presumed that TC synapse strength and reliability can compensate for sparsity[5,6], or that the convergence and synchronous firing of multiple synapses on the same cell can compensate for small synapses[7,8], our findings suggest that neither is the case. We do however show that both TC and CC synapses are more clustered among themselves than expected from a random distribution (see also refs. [18,38,39]). The average nearest-neighbor distance for TC synapses is 9.55 μm as compared to 13.25 μm in the respective random case, and 2.34 μm for CC synapses as compared to 2.48 μm in the respective random case. This 'clustering' brings the distance between TC synapses down below 10 μm, a range shown to enable cooperativity between neighboring synapses for plasticity and memory formation[40,41] (reviewed in ref. [42]). We also found that the basal tree of L2/3 PCs is a preferred target for TC synapses, consistent with speculation by Larkum and colleagues that the separation of feedforward information flow (impinging via TC synapses mostly on the basal tree of L5 PCs) versus feedback information flow (impinging mostly on the apical tuft of L5 PCs) is an important feature of sensory processing[43]. Our study showing that the basal tree of L2/3 PCs is a preferred target site for forward sensory (visual) information suggests that such separation of feedforward and feedback tasks may be a general rule for the cortex.

Since postsynaptic spine volume has been shown to directly correlate with synaptic strength[44], our finding that TC inputs favor smaller spines as compared to CC inputs is seemingly in conflict with the general zeitgeist that TC inputs are stronger than intracortical ones, yet the literature on this not definitive (summarized in Supplementary Table 2). Few papers show a side-by-side comparison of TC versus CC input strength by in vitro, in vivo, intracellular or extracellular physiology. Guo et al. infer that TC drive is stronger than CC inputs, but do not measure unitary synaptic strength, and the study relates to motor rather than sensory thalamic projections[45]. Imaging and EM anatomical side-by-side comparisons are also few, and absolute sizes vary hugely between studies, precluding comparisons across papers. Synapse strength is inferred from either synapse or terminal bouton cross-section size. Yet, a large percentage of thalamic boutons are quite large because they are multisynaptic[19,30], that is, bouton size does not necessarily reflect synapse size. It could also be that variability across

studies reflects differences in thalamic drive depending on target cell regional and laminar location, as well as functional modality. We cannot rule out that the synaptic sizes and distribution patterns that we find are specific to L2/3 PCs of V1.

Our model predicts that albeit their sparseness and small synaptic conductance, L2/3 PCs would typically generate spikes in response to visual input, carried by feedforward TC synapses from the LGN. This is due to balanced background CC and inhibitory synapse activity, which depolarizes the membrane potential sufficiently close to threshold[9,46]. Our model also provides new insight into the decoding style of L2/3 PCs. Due to the large variability in the number and distribution of their excitatory (TC and CC) synapses, the response of individual L2/3 PCs to visual input is expected to be highly noisy and variable. Consequently, the readout of visual features (for example, contrast, frequency) from individual L2/3 PCs is quite poor (Fig. 5). However, visual features could be reliably inferred by a small ensemble consisting of a few scores of these cells (Fig. 6a). Interestingly, recent machine-learning AI studies show that a random feature layer can be highly effective in representing data for subsequent classification tasks[47]. In this context, one may think of each neuron as asking a different question about the visual input and therefore the group of neurons has many answers to many different questions (many different visual features). This computational style is related to the 'wisdom of the crowd' idea, namely the ensemble-based classification approach[48]. This point is specifically emphasized in the present study, where we show that a heterogeneous network of L2/3 neurons achieves high readout accuracy with a smaller number of (costly) TC + CC synapses, as compared to a network composed of homogenous neurons (Fig. 6d). Our results demonstrate that, at the individual-cell level, the more TC synapses the cell receives the better its ability to decode visual parameters. However, when an assembly of neurons is used for the readout, fewer synapses are required for an accurate decoding of the visual feature when using an heterogeneous rather than homogeneous population of neurons. Thus, heterogeneity of synaptic maps imparts a cost advantage in terms of number of synapses required for an accurate readout of the visual input parameters (for example, contrast and frequency). Heterogeneity is an inherent feature of many neuronal systems[49], where various types of (morphological and physiological) heterogeneities serve to reduce system entropy[50], increase computational power[51–53] and provide resilience to perturbation[54,55].

Finally, another unexpected aspect of TC innervation to V1 relates to a highly cited EM study that suggested thalamic afferents are the primary excitatory inputs that co-innervate spines with inhibitory synapses[28]. Analysis of the MAP dataset showed that excitatory inputs on dually innervated spines can be either thalamic or cortical, but are five times more likely to be cortical. This is consistent with the largest spines being dually innervated, and that large spines are more likely to receive cortical input.

In summary, our model predicts that, albeit their relatively low density and small synaptic conductance, feedforward TC synapses are likely to activate, although unreliably, L2/3 PCs following visual input. While the large variability in number and density of TC synapses across different L2/3 PCs implies a large variability in the firing response of these cells to visual input, the activity of a small population of such variable cells enables a reliable readout of different features of the visual input. Sermet et al. show that in both L3 and L4 of somatosensory cortex there is a notable heterogeneity in thalamic drive to individual neurons within the same lamina[13], consistent with our data showing substantial but heterogeneous thalamic innervation onto individual L2/3 PCs in V1. Heterogeneity in the number and distribution of thalamic inputs may therefore be a general feature of TC innervation, and our computational model, which examines how the cortex interprets information from cells that receive heterogeneous inputs, would be applicable across cortical lamina and sensory modalities.

Online content

Any methods, additional references, Nature Portfolio reporting summaries, source data, extended data, supplementary information, acknowledgements, peer review information; details of author contributions and competing interests; and statements of data and code availability are available at https://doi.org/10.1038/s41593-022-01253-9.

References

1. Jones, E. G. Thalamic circuitry and thalamocortical synchrony. *Philos. Trans. R. Soc. Lond. B Biol. Sci.* **357**, 1659–1673 (2002).
2. Halassa, M. M. & Sherman, S. M. Thalamocortical circuit motifs: a general framework. *Neuron* **103**, 762–770 (2019).
3. Douglas, R. J. & Martin, K. A. A functional microcircuit for cat visual cortex. *J. Physiol.* **440**, 735–769 (1991).
4. Douglas, R. J., Koch, C., Mahowald, M., Martin, K. A. C. & Suarez, H. H. Recurrent excitation in neocortical circuits. *Science* **269**, 981–985 (1995).
5. Gil, Z., Connors, B. W. & Amitai, Y. Efficacy of thalamocortical and intracortical synaptic connections: quanta, innervation and reliability. *Neuron* **23**, 385–397 (1999).
6. Stratford, K. J., Tarczy-Hornoch, K., Martin, K. A. C., Bannister, N. J. & Jack, J. J. B. Excitatory synaptic inputs to spiny stellate cells in cat visual cortex. *Nature* **382**, 258–261 (1996).
7. Bruno, R. M. & Sakmann, B. Cortex is driven by weak but synchronously active thalamocortical synapses. *Science* **312**, 1622–1627 (2006).
8. Sedigh-Sarvestani, M., Palmer, L. A. & Contreras, D. Thalamocortical synapses in the cat visual system in vivo are weak and unreliable. *Elife* **8**, e41925 (2019).
9. Wang, H. P., Spencer, D., Fellous, J. M. & Sejnowski, T. J. Synchrony of thalamocortical inputs maximizes cortical reliability. *Science* **328**, 106–109 (2010).
10. Meyer, H. S. et al. Cell type-specific thalamic innervation in a column of rat vibrissal cortex. *Cereb. Cortex* **20**, 2287–2303 (2010).
11. Meyer, H. S. et al. Number and laminar distribution of neurons in a thalamocortical projection column of rat vibrissal cortex. *Cereb. Cortex* **20**, 2277–2286 (2010).
12. Oberlaender, M. et al. Cell-type-specific three-dimensional structure of thalamocortical circuits in a column of rat vibrissal cortex. *Cereb. Cortex* **22**, 2375–2391 (2012).
13. Sermet, B. S. et al. Pathway-, layer- and cell-type-specific thalamic input to mouse barrel cortex. *Elife* **8**, e52665 (2019).
14. Quiquempoix, M. et al. Layer 2/3 pyramidal neurons control the gain of cortical output. *Cell Rep.* **24**, 2799–2807 (2018).
15. Benshalom, G. & White, E. L. Quantification of thalamocortical synapses with spiny stellate neurons in layer IV of mouse somatosensory cortex. *J. Comp. Neurol.* **253**, 303–314 (1986).
16. Peters, A. & Payne, B. R. Numerical relationships between geniculocortical afferents and pyramidal cell modules in cat primary visual cortex. *Cereb. Cortex* **3**, 69–78 (1993).
17. Ahmed, B., Anderson, J. C., Douglas, R. J., Martin, K. A. C. & Nelson, J. C. Polyneuronal innervation of spiny stellate neurons in cat visual cortex. *J. Comp. Neurol.* **341**, 39–49 (1994).
18. Schoonover, C. E. et al. Comparative strength and dendritic organization of thalamocortical and corticocortical synapses onto excitatory layer 4 neurons. *J. Neurosci.* **34**, 6746–6758 (2014).
19. Bopp, R., Holler-Rickauer, S., Martin, K. A. & Schuhknecht, G. F. An ultrastructural study of the thalamic input to layer 4 of primary motor and primary somatosensory cortex in the mouse. *J. Neurosci.* **37**, 2435–2448 (2017).
20. Guillery, R. W. On counting and counting errors. *J. Comp. Neurol.* **447**, 1–7 (2002).
21. Ku, T. et al. Multiplexed and scalable super-resolution imaging of three-dimensional protein localization in size-adjustable tissues. *Nat. Biotechnol.* **34**, 973–981 (2016).
22. Park, J. et al. Epitope-preserving magnified analysis of proteome (eMAP). *Sci. Adv.* **7**, eabf6589 (2021).
23. Subramanian, J., Michel, K., Benoit, M. & Nedivi, E. CPG15/neuritin mimics experience in selecting excitatory synapses for stabilization by facilitating PSD95 recruitment. *Cell Rep.* **28**, 1584–1595 (2019).
24. Villa, K. L. et al. Inhibitory synapses are repeatedly assembled and removed at persistent sites in vivo. *Neuron* **89**, 756–769 (2016).
25. Fremeau, R. T. Jr. et al. The expression of vesicular glutamate transporters defines two classes of excitatory synapse. *Neuron* **31**, 247–260 (2001).
26. Balaram, P., Hackett, T. A. & Kaas, J. H. Differential expression of vesicular glutamate transporters 1 and 2 may identify distinct modes of glutamatergic transmission in the macaque visual system. *J. Chem. Neuroanat.* **50-51**, 21–38 (2013).
27. Roth, M. M. et al. Thalamic nuclei convey diverse contextual information to layer 1 of visual cortex. *Nat. Neurosci.* **19**, 299–307 (2016).
28. Kubota, Y., Hatada, S., Kondo, S., Karube, F. & Kawaguchi, Y. Neocortical inhibitory terminals innervate dendritic spines targeted by thalamocortical afferents. *J. Neurosci.* **27**, 1139–1150 (2007).
29. Nahmani, M. & Erisir, A. VGluT2 immunochemistry identifies thalamocortical terminals in layer 4 of adult and developing visual cortex. *J. Comp. Neurol.* **484**, 458–473 (2005).
30. Rodriguez-Moreno, J. et al. Quantitative 3D ultrastructure of thalamocortical synapses from the 'lemniscal' ventral posteromedial nucleus in mouse barrel cortex. *Cereb. Cortex* **28**, 3159–3175 (2018).
31. Banitt, Y., Martin, K. A. & Segev, I. A biologically realistic model of contrast invariant orientation tuning by thalamocortical synaptic depression. *J. Neurosci.* **27**, 10230–10239 (2007).
32. Huang et al. Relationship between simultaneously recorded spiking activity and fluorescence signal in GCaMP6 transgenic mice. *eLife* **10**, 1–19 (2021).
33. Shamir, M. Emerging principles of population coding: in search for the neural code. *Curr. Opin. Neurobiol.* **25**, 140–148 (2014).
34. Hung, C. P., Kreiman, G., Poggio, T. & DiCarlo, J. J. Fast readout of object identity from macaque inferior temporal cortex. *Science* **310**, 863–866 (2005).
35. Yan, Y. et al. Perceptual training continuously refines neuronal population codes in primary visual cortex. *Nat. Neurosci.* **17**, 1380–1387 (2014).
36. Berens, P. et al. A fast and simple population code for orientation in primate V1. *J. Neurosci.* **32**, 10618–10626 (2012).
37. Heyer, D. B. et al. Verbal and general IQ associate with supragranular layer thickness and cell properties of the left temporal cortex. *Cereb. Cortex* **32**, 2343–2357 (2022).
38. Rah, J. C. et al. Thalamocortical input onto layer 5 pyramidal neurons measured using quantitative large-scale array tomography. *Front Neural Circuits* **7**, 177 (2013).
39. Bagnall, M. W., Hull, C., Bushong, E. A., Ellisman, M. H. & Scanziani, M. Multiple clusters of release sites formed by individual thalamic afferents onto cortical interneurons ensure reliable transmission. *Neuron* **71**, 180–194 (2011).
40. Harvey, C. D. & Svoboda, K. Locally dynamic synaptic learning rules in pyramidal neuron dendrites. *Nature* **450**, 1195–1200 (2007).
41. Engert, F. & Bonhoeffer, T. Synapse specificity of long-term potentiation breaks down at short distances. *Nature* **388**, 279–284 (1997).
42. Kastellakis, G. & Poirazi, P. Synaptic clustering and memory formation. *Front Mol. Neurosci.* **12**, 300 (2019).

43. Suzuki, M. & Larkum, M. E. General anesthesia decouples cortical pyramidal neurons. *Cell* **180**, 666–676 (2020).

44. Holler, S., Kostinger, G., Martin, K. A. C., Schuhknecht, G. F. P. & Stratford, K. J. Structure and function of a neocortical synapse. *Nature* **591**, 111–116 (2021).

45. Guo, Z. V. et al. Maintenance of persistent activity in a frontal thalamocortical loop. *Nature* **545**, 181–186 (2017).

46. Wang, H. P., Garcia, J. W., Sabottke, C. F., Spencer, D. J. & Sejnowski, T. J. Feedforward thalamocortical connectivity preserves stimulus timing information in sensory pathways. *J. Neurosci.* **39**, 7674–7688 (2019).

47. Rahimi, A. & Recht, B. Random features for large-scale kernal machines. in *Proceedings of the 20th International Conference on Neural Information Processing Systems* (eds. J. C. Platt et al.) 1177–1184 (Curran Associates, 2008).

48. Rokach, L. Ensemble-based classifiers. *Artif. Intell. Rev.* **33**, 1–39 (2010).

49. Marder, E. Variability, compensation, and modulation in neurons and circuits. *Proc. Natl Acad. Sci. USA* **108**, 15542–15548 (2011). Suppl 3.

50. Reimann, M. W., Horlemann, A. L., Ramaswamy, S., Muller, E. B. & Markram, H. Morphological diversity strongly constrains synaptic connectivity and plasticity. *Cereb. Cortex* **27**, 4570–4585 (2017).

51. Padmanabhan, K. & Urban, N. N. Intrinsic biophysical diversity decorrelates neuronal firing while increasing information content. *Nat. Neurosci.* **13**, 1276–1282 (2010).

52. Tripathy, S. J., Padmanabhan, K., Gerkin, R. C. & Urban, N. N. Intermediate intrinsic diversity enhances neural population coding. *Proc. Natl Acad. Sci. USA* **110**, 8248–8253 (2013).

53. Mejias, J. F. & Longtin, A. Optimal heterogeneity for coding in spiking neural networks. *Phys. Rev. Lett.* **108**, 228102 (2012).

54. Ramaswamy, S. et al. Intrinsic morphological diversity of thick-tufted layer 5 pyramidal neurons ensures robust and invariant properties of in silico synaptic connections. *J. Physiol.* **590**, 737–752 (2012).

55. Rich, S., Moradi Chameh, H., Lefebvre, J. & Valiante, T. A. Loss of neuronal heterogeneity in epileptogenic human tissue impairs network resilience to sudden changes in synchrony. *Cell Rep.* **39**, 110863 (2022).

Methods

Animals

All animal procedures were approved by the Institutional Animal Care and Use Committees at the Massachusetts Institute of Technology and University of Virginia, and meet the National Institutes of Health (NIH) guidelines for the use and care of vertebrate animals. Transgenic Olig3-Cre mice[56] were a kind gift from Y. Nakagawa at the University of Minnesota. Two cell embryos were received and implanted in pseudo-pregnant foster mice. The colony, derived from eight founders, was maintained by breeding heterozygous (Het) males and females. For labeling thalamic axonal boutons, Het Olig3-Cre female mice were crossed to homozygous synaptophysin-Tdtomato (synTd) males (Jackson, 012570), which express the presynaptic marker synaptophysin fused to Tdtomato in a Cre-dependent manner. Ai14 mice (Jackson, 007914) were used for confirming Olig3-Cre thalamic specificity. All mice were on the C57BL/6 background, were aged approximately 2 months and comprised an equal number of males and females. Mice were housed in standard static caging with hardwood bedding with 12-h/12-h lighting, 07:00 sunrise and 19.00 sunset, and room temperature (RT) maintained at 70 °F ± 2 °F and 30–70% humidity.

DNA constructs

Generation of the Flp-dependent *eYFP* and *PSD95–Teal* plasmids (*pFudioFRTeYFPW*; Addgene plasmid no. 133998 and *pFudioFRTPSD95TealW*; Addgene plasmid no. 134299, respectively) has been previously described[23]. The plasmid expressing Flp recombinase (*pPGKFLPobpA*; Addgene plasmid no. 13793) was a gift from P. Soriano[57].

Surgical procedures

To label L2/3 cortical pyramidal neurons, in utero electroporation was performed as previously described[58] on timed pregnant Olig3/+ females (from cross to SynTd$^{+/+}$ males). At E15.5, 0.75 μl of plasmid solution containing *pFudioFRTeYFPW, pFudioFRTPSD95TealW* and *pPGK-FLPobpA*, with 0.1% Fast Green for visualization, was injected into the pups' right lateral ventricle with a 32-gauge Hamilton syringe (Hamilton Company). To achieve the sparse labeling optimal for single-neuron imaging with high incidence of fluorophore coexpression, plasmid molar ratios were high for fluorophore constructs and limiting for the recombinase[23,24,59], with constructs expressing eYFP, PSD95–Teal and Flp at a ratio of 10:5:0.2, respectively (total DNA concentration 1.2 mg ml^{-1}). A pair of 5-mm-diameter platinum electrodes (Protech International) were used to deliver five pulses of 36 V (duration 50 ms, frequency 1 Hz) from a square-wave electroporator (ECM830, Harvard Apparatus) targeting the visual cortex. Pups born after in utero electroporation were reared to adulthood, and at around postnatal day (P) 42 were implanted with a 5-mm glass coverslip replacing a skull area over the occipital cortex in the right hemisphere, as previously described[60]. Following cranial window placement surgery, mice were housed individually with sulfamethoxazole (1 mg ml^{-1}) and trimethoprim (0.2 mg ml^{-1}) in the drinking water to retain optical clarity of the implanted windows[60].

Optical intrinsic signal imaging

To map binocular visual cortex, optical imaging of intrinsic signal and data analysis were performed as described previously[61]. Mice were anesthetized and maintained on 0.25–0.75% isoflurane and secured in a stereotaxic frame. A horizontal bar (5° in height and 73° in width) drifting upward with a periodicity of 12 s was presented for 60 cycles on a high-refresh-rate monitor 25 cm in front of the animal, first to the eye ipsilateral to the window, and then the contralateral eye. Optical images of visual cortex were acquired continuously under 610 nm of illumination with an intrinsic imaging system (LongDaq Imager 3001/C, Optical Imaging) through a ×2.5/0.075-NA objective (Zeiss). Images were spatially binned by 4 × 4 pixels for analysis, and cortical intrinsic signal was computed by extracting the Fourier component of light-reflectance changes matched to stimulus frequency. Response magnitude was the fractional change in reflectance, and the magnitude maps were thresholded at 30% of peak-response amplitude. Binocular visual cortex was defined by the response to stimulation of the eye ipsilateral to the window.

In vivo two-photon imaging

Following cranial window surgery, mice recovered for 2 weeks allowing optical clearing and cessation of potential inflammation[60]. Labeled cells in binocular visual cortex were then screened for the presence of both fluorescent labels. Well-isolated cells with 200–300 somatic photon counts in the green channel were imaged from nine anesthetized (0.75–1.25% isoflurane) head-fixed mice using a custom-built two-photon microscope with custom acquisition software to enable triple-color imaging (eYFP for cell fill, PSD95–Teal for postsynaptic excitatory synapses, and synTd for presynaptic thalamic boutons). Cells with excessive labeling were not used for experiments. Only one cell was imaged per animal. Fluorophores were simultaneously excited using a commercial Mai Tai HP Ti: Sapphire laser (Spectra-Physics) at 915 nm. A volume of 192 × 192 × 200 μm was scanned at a resolution of 250 nm/pixel by steering the laser beam with galvanometric *xy*-scanning mirrors (6215H, Cambridge Technology) and a z-resolution of 0.9 μm/frame was achieved using a piezo actuator (Piezosystem, Jena). The laser beam was focused by a ×20/1.0-NA water-immersion objective lens (W Plan-Apochromat, Zeiss), with the power delivered to the specimen ranging from 35 to 50 mW depending on imaging depth, to collect approximately 30 photon counts per fluorophore on dendrites and boutons. The emission signals were collected using the same objective lens and passed through an IR blocking filter (E700SP, Chroma Technology), then spectrally separated using dichroic mirrors at 520 nm and 560 nm. Emission signals were simultaneously collected onto three independent photomultiplier tubes after passing through appropriate bandpass filters (485/70, 550/100 and 605/75).

Data analysis, statistics and reproducibility (in vivo imaging)

Two-photon raw data were processed for spectral linear unmixing as described previously[23,24], and the images were converted to an RGB image z-stack using MATLAB and ImageJ (NIH). Dendritic segments, PSD95-containing spines and thalamic boutons were scored manually with a custom-written four-dimensional (4D) point-tracking system implemented in Fiji[62] using a modified version of ObjectJ plugin (https://sils.fnwi.uva.nl/bcb/objectj/index.html). Analysis was performed by one investigator and independently confirmed by a second investigator. No data were excluded from analysis. Because of the bright labeling on the soma and proximal dendrites, individual contacts in these regions could not be resolved, and analysis was restricted to dendrites starting approximately 40 μm from the soma and extending to the most distal tips contained within the imaging volume. Dendritic spine scoring was as defined previously[59], protrusions of at least three pixels present in two consecutive z-planes. Z-projecting spines were excluded from analysis. PSD95 puncta were scored as synapses if at least four pixels were present in two consecutive z-planes, or eight to nine pixels in one z-plane (0.27 μm^2 in size), with a minimal average signal intensity at least four times above shot noise. Previous EM validation confirmed that these criteria represent excitatory synapses[24]. Thalamic boutons were defined by the presence of nine synTd pixels in two consequent z-planes. Dendritic arbors were manually traced in Neurolucida 360 (MicroBrightField) to quantify the length of scored branches. Nine cells were scored with cell bodies ranging in depth from 89 to 208 μm from the pia. We tracked 2,419 excitatory synapses on 113 dendritic segments. These included 70 basal and 43 apical dendrites, with a combined branch length of 8,930 μm, of which 5,620 μm was for basal and 3,310 μm for apical dendrites, with at least 25 synapses counted per branch, and at least 300 counted per animal. Sample size was based on previously published work[23,24].

Dendrograms were prepared using Neurolucida 360 for tracing and 3D visualization. After tracing, the coordinates of the

PSD95-containing synapses were superimposed onto the 3D dendrite skeleton, and Neurolucida 360 Explorer was used to create the respective dendrograms, which were then exported into Adobe Illustrator for visual presentation.

To assess local bouton density versus synaptic contacts per branch (Extended Data Fig. 8), nine dendritic branches from four neurons were selected to sample the cortical depth from the most superficial to the deepest in vivo-imaged neurons. Boutons surrounding each branch were counted in the Syntd channel, blind to depth, and to location of the branch in the volume. Then, 4 × 4-µm regions of interest (ROIs) were placed around each branch in the three z-planes where the branch was brightest. The ROIs were then overlayed onto the bouton channel, and boutons within the ROIs were counted as 'local boutons'. Correlation between branch depth and local bouton density was tested by linear regression to determine goodness of fit (R^2).

Synaptic clustering was assessed by comparing the mean distance between synapses when placed in random dendritic locations to the actual distribution of synapses as found on the nine neurons imaged in vivo in their entirety. For the biological case, the number of TC and CC synapses on each dendritic branch was counted and the mean distance between these synapses was measured. To compute the respective random cases, we randomly shuffled between locations of the TC and CC synapses on each dendrite. We repeated this process 10,000 times per cell. In each case, we calculated the distance between each synapse to its nearest neighbor on the same branch, resulting in a list of 10,000 distances to the nearest neighbor for each synapse. This provided the mean distance and standard deviation, to the nearest neighbor in the random case. Biological mean distance (clustering) was assessed using a Student's t-test for TC synapses, CC synapses, as well as for the distance between TC synapses to the nearest CC synapse in both experiments and the random case.

Histology and immunohistochemistry

To test the fidelity of thalamus-specific Cre-mediated recombination, Het Olig3-Cre females were crossed to $Ai14^{+/+}$ Tdtomato reporter males. Three-month-old F1 Olig3/+ mice from this cross were perfused transcardially with PBS, followed by 4% paraformaldehyde (PFA). Brains were removed and post-fixed overnight in 4% PFA at 4 °C. Fifty-micrometer sections containing visual cortex were cut using a vibratome (Leica VT1000S), then mounted on slides using Fluoromount-G (SouthernBiotech) for visualization, or processed for immunohistochemistry. For direct visualization, images were collected on an upright epifluorescence scope with ×1/0.04-NA and ×20/0.3-NA objectives (Nikon Eclipse E600) at different Bregma coordinates on the anteroposterior axis. Images were processed using ImageJ (NIH).

For assessing bouton density as a function of dendritic branch depth (Extended Data Fig. 8), coronal sections through visual cortex were stained with DAPI, mounted on slides using Fluoromount-G (SouthernBiotech), then 100 × 250-µm columns were imaged using a confocal microscope (Olympus FV1200) with a ×60/1.3-NA objective. Olig3 boutons per bin were counted using ImageJ's watershed and Analyze Particles functions with a size criterion of 0.3 to 3 µm.

For immunohistochemistry, sections were blocked for 2 h in solution containing 10% normal goat serum (NGS) or 10% fetal calf serum (FCS) and 1% Triton X-100, then incubated overnight at 4 °C in a solution containing PBS, 5% NGS or FCS, and 0.1% Triton X-100 and primary antibodies against VGlut2 AB2251-I (1:5,000 dilution, guinea pig polyclonal; Millipore) and GFP Ab290 (1:3,000 dilution, rabbit polyclonal; Abcam). Sections were washed three times in PBS, then incubated with a secondary antibody solution containing PBS, 5% NGS or FCS, and 0.1% Triton X-100 and secondary antibodies conjugated to Alexa 647 (1:400 dilution, anti-guinea pig IgG; Nanotag) or Alexa 488 (1:400 dilution, anti-rabbit IgG; Invitrogen) for 2 h. Sections were washed three times in PBS and mounted on slides using Fluoromount-G (SouthernBiotech). Images were collected on an upright epifluorescence scope (Nikon

Eclipse E600) using a ×20/0.75-NA objective (Nikon). For each section, images of the same visual cortex area and focal plane were taken using the GFP (green) and Alexa 647 (far red) channels. ImageJ (NIH) was used to identify double-labeled cells within each layer.

Electron microscopy tissue preparation

Three adult mice (C57BL/6) were given an overdose of anesthetics (Euthasol (pentobarbital sodium and phenytoin sodium) 300 mg per kg body weight), then perfused transcardially with Tyrodes solution (137 mM NaCl, 5.5 mM dextrose/glucose, 1.2 mM $MgCl_2$, 2 mM KCl, 0.4 mM NaH_2PO_4, 0.9 mM $CaCl_2$, 11.9 mM $NaHCO_3$, in ultrapure H_2O, RT, 1–2 min) followed by 100 ml of 4% PFA, and 0.5% in 0.1 M phosphate buffer (pH 7.4). Brains were removed and post-fixed overnight in the fixative solution at 4 °C. Then, brains were sectioned at 60 µm using a vibratome (Leica), and incubated in anti-guinea pig VGluT2 (Millipore Bioscience Research Reagents, AB2251-I, RRID: AB_1587626) at a concentration of 1:5,000 in PBS containing 1% bovine serum albumin and 0.05% NaN). Sections were then incubated with a secondary antibody solution (biotinylated anti-guinea pig, 1:100 dilution), followed by treatment with avidin and biotin (ABC; Vector), for 2 h each. The tissue was then rinsed in 0.01 M PBS and incubated in a solution of hydrogen peroxide and 0.05% diaminobenzidine for 3–7 min. For resin embedding of immunostained sections, routine protocols were used: The sections counterstained with 1% osmium tetroxide in 0.1 M phosphate buffer for 1 h, and in filtered 4% uranyl acetate in 70% alcohol overnight. They were then dehydrated in a series of alcohol and acetone, and they were gradually infiltrated with resin (Embed 812, EMS), overnight. Sections were then flat embedded between two Aclar sheets (EMS), and were cured in a 60 °C oven for 1–2 d. Sections containing V1 were excised, placed in BEEM capsules (EMS), and they were repolymerized. The area of interest on each capsule was trimmed to a 1 mm by 2 mm trapezoid, usually containing a strip between the pial surface and the white matter. Ultrathin sections of 50–80-nm thickness were cut at the tissue-Epon interface zone (that is, containing the top 2–5 µm of the 50-µm-thick sections, where the antibody can penetrate), and collected on 200 mesh copper grids (Ted Pella) using an ultramicrotome (Ultracut UCT7; Leica). The ultrathin sections were examined on a JEOL 1010 electron microscope, starting from the pial surface, and moving toward the deeper layers. L2/3 was identified as the cell-dense layer next to the cell-sparse neuropil of layer 1. The tissues containing VGluT2$^+$ terminals were imaged as they were encountered during systematic examination of the tissue, using a 16-Mpixel CCD camera at ×12,000 magnification, yielding a resolution of <2pixels/nm, that is sufficient for clear visualization of lipid bilayer.

Electron microscopy data analysis, statistics and reproducibility

Image Pro Plus 7 (Media Cybernetics) was used to examine a total of 24 images from two EM blocks obtained from two brains, and to measure the cross-sectional terminal area, spine area and synapse length at VGluT2$^+$ and unlabeled axo-spinous synapses. The third brain was not imaged due to suboptimal ultrastructural preservation. These images yielded a dataset that included 94 axo-spinous synaptic terminals, 33 of which were identified as thalamic in origin based on the VGluT2 label. No statistical method was used to determine thalamic and cortical terminal sample sizes: these were determined by the random occurrence probability of axo-spinous synapses and their labeling status. As such, no blinding was possible for group allocations. No data points were excluded from analysis. Non-parametric statistical tests, including Mann–Whitney U tests and descriptive statistics were performed using Prism software (GraphPad). As the area measurements of 3D objects are expected to have non-normal distribution, and terminals from different origins may have different phenotypical morphometry and unequal variances, the data met the assumptions of the descriptive statistical tests used. The dataset of spine/terminal

area ratio measurements met the assumptions of the non-parametric Mann–Whitney U test (two-tailed).

Magnified analysis of proteome tissue processing

Immediately following in vivo two-photon imaging, brains were perfused with cooled PBS followed by 4% PFA through transcardial perfusion. Brains were then extracted and post-fixed in the same fixative solution at 4 °C for 1 d, and then for 3 h at RT with gentle shaking. The protocol was optimized for later experiments to omit the 3-h post-fixation step at RT for improved antigen preservation. Brains were then washed in PBS at 4 °C for 1 d, and then RT for 1 d. A rough ~2-mm section horizontal to the former location of the cranial window was cut by hand using a razor blade.

The original MAP protocol[21] was modified based on physical hybridization of tissue with a dense hydrogel[63] as follows. Two stock solutions were prepared: a MAP stock solution and an initiator stock solution. The MAP stock solution was prepared by dissolving 30% (wt/vol) acrylamide (A9099; MilliporeSigma), 10% (wt/vol) sodium acrylate (408220; MilliporeSigma) and 0.1% bisacrylamide (161-0142; Bio-Rad Laboratories) in PBS, then stored at 4 °C protected from light. The initiator stock solution was prepared by dissolving 10% (wt/vol) VA-044 (Wako Chemicals) in ice-cooled deionized water, and stored in aliquots at −20 °C. For each MAP-processing sample, the ~2-mm-thick section was placed in a 15-ml conical tube containing ice-cold MAP solution made by adding 36 µl of thawed initiator stock to 12 ml MAP stock. The tube was then incubated overnight at 4 °C with gentle shaking. For gelation, a Blu-Tack adhesive (Bostik, Essendon Fields) was shaped into a ~4-mm-thick strip and put on a glass slide to make a U-shaped chamber. After firmly attaching the strip to the slide glass, the sample was placed in the center of the chamber avoiding bubble trapping between the sample and the glass. A drop of the MAP solution used for sample incubation was applied to top of the sample, which was then covered by a second slide glass, again avoiding bubble trapping. The two glass slides were gently compressed until both were contacting the sample, and the Blu-Tack strip was firmly attached to both. The chamber was filled with MAP solution with bubbles removed by gentle tapping, then the open edge of the cartridge was secured with plastic tape. The cartridge was inserted into a 50-ml conical tube, and nitrogen gas was used to purge the air before capping with a metal screw cap connected to a nitrogen gas cylinder. The tube was then left at 36–37 °C for 2.5 h, resting at a low angle (approximately 15°). After gelation, the cartridge was disassembled, excess gel was trimmed, and the tissue–gel hybrid sample was placed in PBS at 37 °C overnight for hydration. At this point, the sample was ~1.7 times the original size in all directions, and the endogenous YFP cell fill fluorescence was still preserved.

The MAP-processed sample was further sectioned on a vibratome to preserve a ~500 µm-to-1 mm section of the brain surface underneath the former location of the cranial window. Tiled GFP epifluorescence images of the resulting section were then obtained on a TissueFAXS slide scanning system to generate a blood vessel map. The location of the cell formerly imaged in vivo was identified in the sample by aligning the blood vessel map generated by the slide scanner with the blood vessel map observed through the cranial window at the time of in vivo imaging. In some cases, tiled confocal z-stacks of the ROI were collected on an Olympus FV1200 microscope with a ×20/1.0-NA water-immersion objective and 488-nm laser excitation, to confirm cell identity. Once the target cell was identified, the sample was glued to a vibratome chuck, and trimmed in the x and y planes, frequently checking the location of the target cell by placing the chuck under the Olympus FV1200 microscope. The three cells imaged for MAP inhibitory synapse labeling were not previously imaged in vivo, but were localized to L2/3 V1 based on stereotaxic coordinates before trimming. Samples were then further sectioned on the vibratome to obtain a thin section, varying from 100 to 510 µm in thickness, centered around the target cell body. Sections were cut as thin as possible, to optimize antibody penetration, while

at the same time maintaining as many branches as possible within the accessible working distance of the MAP imaging objective.

The trimmed sample was incubated for 4–6 h at 37 °C in 12-ml clearing solution (6% (wt/vol) sodium dodecyl sulfate (75746; MilliporeSigma), 50 mM sodium sulfite (S0505; MilliporeSigma) and 0.02% (wt/vol) sodium azide (S2002; MilliporeSigma) in 0.1 M phosphate buffer, with pH adjusted to 7.4). The sample was then transferred using a fine paintbrush into 17.5 ml of clearing solution pre-heated to ~86 °C in a 95 °C environment. After 10 min, the sample was quickly transferred into RT washing solution (PBST - 0.1% (wt/vol) Triton X-100 in 1× PBS with 0.02% (wt/vol) sodium azide) for at least 6 h at 37 °C with one change of the washing solution.

Immunostaining of magnified analysis of proteome-processed tissue

The MAP-processed trimmed section containing the target cell was incubated with primary antibodies in 500 µl to 1 ml PBST at RT for 1–4 d, followed by washing at RT in PBST three times over 6–24 h. The section was then incubated with secondary antibodies in 300–500 µl PBST at RT for 1–2 d, followed by washing at RT in PBST three times over 6–24 h. Primary antibodies were directed against VGluT2 (AB2251-I; MilliporeSigma), VGluT1 (135 302; Synaptic Systems), PSD95 (73-028; UC Davis/NIH NeuroMab Facility), Bassoon (141 004 and 141 003; Synaptic Systems), GFP (A10262; Thermo Fisher Scientific), RFP (600-401-379; Rockland) and Gephyrin (612632; BD Biosciences). See Supplementary Table 3 for the list of secondary antibodies used. Of the six cells imaged for MAP that were previously imaged in vivo, five were de-stained for a second round of labeling. De-staining followed a similar protocol to the clearing procedure. The sample was incubated in a 12-ml clearing solution at 37 °C for 2 h and then incubated in a 17.5-ml pre-heated clearing solution for 30 min. The de-stained sample was washed with PBST at 37 °C for 4–6 h with exchanging the solution once. VGluT1 and VGluT2 primary antibodies were always included in round 1, as the antigenicity of these vesicular antigenic targets can be lost in the de-staining. Anti-GFP was included in each round to label the cell fill for registration between rounds and with two-photon images. High concentrations of both primary and secondary antibodies were used with the goal of saturating all antigen targets throughout the sample. The typical volumes of primary antibodies used were as follows: VGluT2 (10–30 µl), VGluT1 (20–40 µl), PSD95 (15–20 µl), Bassoon (10–40 µl), GFP (5–10 µl), RFP (10–40 µl) and Gephyrin (10 µl). Secondary antibodies were used at the same volume of the corresponding primary antibody, with the exception of the secondary antibody for anti-GFP, which was used at two times the volume of the primary antibody.

The immunostained section was then further expanded in dilute buffer (either 0.005-0.02 × PBS, or 0.1 mM Tris (RDD008; MilliporeSigma)−0.02 × PBS was preferred when there was concern for loss of primary antibody binding over prolonged imaging sessions, in particular for anti-VGluT2 and anti-VGluT1, Tris buffer was used for the more stable primary antibodies) and allowed to stabilize for at least 1 h before imaging. Expansion ratios for the different cells ranged from 3.1 to 4.2 times the expansion in all directions, with expansion ratio defined as the dendritic length in the MAP-processed confocal images divided by the dendritic length from the in vivo two-photon images, both reconstructed in Neurolucida 360.

Expanded samples were mounted on a 60-mm-diameter Petri dish and covered with a glass-bottom Willco dish (HBSB-5030; WillCo Wells) secured with Blu-Tack adhesive. The space between the Willco dish and Petri dish, and surrounding the sample, was filled with expansion buffer. MAP samples were then imaged on a Leica TCS SP8 microscope system with a ×63/1.30-NA glycerol-immersion objective with a white-light tunable laser source. Individual dendrites were selected for MAP imaging based on adequate antibody labeling, and accessibility given the working distance of the objective, with preference for dendrites located within a continuous xy plane. Images of

individually selected dendrites were acquired with resolutions of 75 nm/pixel (*xy*) and 0.66 µm/frame (*z*). Wide-field whole-cell images of the anti-GFP-labeled channel were also obtained by *z*-stack acquisition with a ×10/0.3-NA water-immersion objective.

Magnified analysis of proteome analysis, statistics and reproducibility

MAP images were scored manually using a modified version of the ObjectJ 4D point-tracking system plugin for Fiji/ImageJ[62]. MAP images were first processed to decrease noise using the ImageJ smooth command. The display range for each channel was then manually adjusted linearly. Dendrites in the MAP images were registered to the same dendrites in the two-photon in vivo image. Dendritic spines that were not visible, or that did not contain PSD95 on the two-photon in vivo image, were excluded from MAP analysis. Dendritic spines in the MAP images were then assessed for their presynaptic partner bouton, either thalamic (boutons labeled with either anti-VGluT2 or anti-RFP, to label Synaptophysin-tdTomato) or intracortical (boutons labeled with VGluT1). Labeled PSD95 and/or Bassoon were considered markers of the physical synapse. All cells successfully immunostained and imaged for MAP were analyzed. No statistical method was used to predetermine sample size. For the MAP inhibitory synapse labeling experiment, all dendritic spines that contained an excitatory synapse (defined as presence of Bassoon not apposed to Gephyrin) were analyzed for the presence of an inhibitory synapse on the same dendritic spine (defined as Bassoon apposed to Gephyrin).

Neurolucida 360 was used for morphometric modeling of dendritic spines to obtain dendritic spine volume[64]. MAP-imaged dendrites that contained at least one dendritic spine with a thalamic synapse were analyzed for dendritic spine volume. The MAP image channel containing the anti-GFP cell fill staining for the dendritic segments was first processed with the Neurolucida 360 Closing filter. Next, the dendritic segments were reconstructed using the user-guided, typically voxel scooping method. The click-to-detect method was used to detect dendritic spines using an outer range of 15 µm, minimum height default and minimum count of 100 voxels. The filter image noise option was selected. The detector sensitivity was adjusted until the spine modeling algorithm best detected individual dendritic spines. After dendritic spine modeling was complete, Neurolucida Explorer was used to generate data files with dendritic spine volume. Spine volume was normalized to a fourfold expansion to accommodate differing degrees of expansion between MAP samples, and then divided by 64 (4^3) to convert to an unexpanded value that more closely approximates a physiological volume. Dendritic spine volume data were analyzed using a two-way ANOVA in GraphPad Prism. Data variances were assumed to be equal but this was not formally tested.

MAP measurements for comparison with EM were done using Neurolucida 360. A single *x*–*y* plane through the dendritic spine head that contained PSD95 was selected using a random number generator, with anti-VGluT2 or anti-VGluT1 marking bouton area. Spine head and bouton were then manually outlined using the contour tool. Due to the need to outline the bouton, analysis could not be performed blind.

Detailed biophysical modeling of a L2/3 pyramidal neuron

Since we did not have electrophysiological measurements from our nine reconstructed L2/3 cells, we complemented our anatomical/synaptic data with the respective biophysical and morphological measurements from the same cell types as provided by the Allen Institute database (http://celltypes.brain-map.org/). Based on this dataset, we constructed a detailed biophysical model for a prototypical L2/3 mouse pyramidal neuron from V1 (Extended Data Fig. 6 and Fig. 5). The criteria for selecting a particular cell from the Allen Institute database were as follows: The cell should be a L2/3 PC from the Cux2ERT2 mouse line from area V1, with fully reconstructed dendritic tree and a large set of electrical measurements, both subthreshold and suprathreshold. From the few cells that matched these criteria, we selected

one cell whose morphology was the most similar to that of our cells (cell no. 517319635; http://celltypes.brain-map.org/experiment/electrophysiology/517319635/).

This cell's morphology was imported into the NEURON simulation[65]; we then used the subthreshold and suprathreshold measurements from this cell as a target for the biophysical L2/3 cell model[66]. First, using Praxis (PRinciple Axis) optimization[67], we fitted the passive properties of the cell such that the model response would match the experimental response for both a brief and a set of prolonged depolarizing current pulses (Extended Data Fig. 9a,b). This provided an axial resistance (R_a) of 100 Ωcm, specific membrane capacitance (C_m) of 2 µF/cm² and specific membrane resistance (R_m) of 10,505 Ωcm². To compensate for the membrane area of the dendritic spines, without modeling them explicitly, we adjusted the specific capacitance and membrane resistance using the *F*-factor method[68] defined according to equation (1):

$$F = (\text{area}_{\text{dend}} + \text{area}_{\text{spines}}) / \text{area}_{\text{dend}} \tag{1}$$

where area$_{\text{dend}}$ is the area of the dendrites (without the spines) and area$_{\text{spines}}$ is the membrane area of the spines. Compensation for the presence of dendritic spines is then implemented by changing the specific membrane resistivity and capacitance, R_m and C_m, according to equation (2):

$$R'_m = R_m/F, \; ; \; C'_m = C_m \times F \tag{2}$$

Based on our measurements, the *F* factor for our modeled cell was 1.17.

Next, we fitted the excitable/firing properties of the cell (Extended Data Fig. 9c) for which we used the multiple objective optimization algorithm[69] to determine the densities of a set of nonlinear membrane ion channels that give rise to the observed experimental recordings. Supplementary Table 1 summarizes the channels and parameters that best fit the experimental results.

Fitting thalamocortical synaptic conductance to experimental results

As a target for fitting TC synapse conductance, we used two datasets from the literature. As there are no measurements of the L2/3 PC somatic excitatory postsynaptic potential (EPSP) in response to a single thalamic axon, we used the unitary EPSP measured in vivo following the activation of a single thalamic axon impinging on an L4 PC[7] (and see also recent work by Sedigh-Sarvestani et al.[8]) The average peak amplitude of this unitary EPSP was found to be ~0.5 mV (Extended Data Fig. 9d). The average number of synaptic contacts that a single TC axon makes on L4 PC is seven[70]. To estimate what would be the synaptic conductance per synaptic contact that would give rise to the experimental EPSP, we used a biophysical model of an L4 pyramidal cell from the Blue Brain Project (https://bbp.epfl.ch/nmc-portal/microcircuit#/mtype/L4_PC/)[70], then placed seven synaptic contacts over its dendritic tree at random locations, and activated them simultaneously, measuring the resultant somatic EPSP (Extended Data Fig. 9d).

The synaptic current I_{syn} was modeled according to equation (3):

$$I_{syn} = g_{syn}(t, V) \times (V - E_{syn}) \tag{3}$$

where $g_{\text{syn}}(t, V)$ is the synaptic conductance change and E_{syn} is the reversal potential for the synaptic current. E_{syn} was set to 0 mV for both the AMPAR-mediated and the NMDAR-mediated currents.

The synaptic conductance, for both AMPA and the NMDA components, was modeled using two-state kinetic synaptic models, with rise time (τ_{rise}) and decay time (τ_{decay}) constants given by equation (4):

$$g_{syn}(t, V) = B \times g_{\max} \times N \times (\exp(-t/\tau_{decay}) - \exp(-t/\tau_{rise})) \tag{4}$$

Here g_{max} denoted below as $\bar{g}_{AMPA}$ and $\bar{g}_{NMDA}$ for AMPA and NMDA conductances, respectively, is the maximal synaptic conductance and N is a normalization factor given by equation (5):

$$N = \frac{1}{\exp\left(-t_{rise}/\tau_{decay}\right) - \exp\left(-t_{peak}/\tau_{rise}\right)} \quad (5)$$

and t_{peak} (time to peak of the synaptic conductance) is given by equation (6):

$$t_{peak} = \frac{\tau_{rise} \times \tau_{decay}}{\tau_{decay} - \tau_{rise}} \times \log\left(\frac{\tau_{decay}}{\tau_{rise}}\right). \quad (6)$$

We used $\tau_{rise} = 0.2$ ms and $\tau_{decay} = 1.7\ ms$ for the AMPA conductance[71], and $\tau_{rise} = 2\ ms$ and $\tau_{decay} = 75\ ms$ for the NMDA conductance[72]. The voltage dependence of the NMDA conductance is implemented by the factor B in equation (4) as in ref. [73]:

$$B = \frac{1}{1 + \exp\left(-\gamma \times V\right) \times [Mg^{2+}] \times n} \quad (7)$$

$[Mg^{2+}]$ was fixed at 1 mM, $\gamma = 0.08$ (1/mV)[74] and $n = 0.27$ (1/mM) and $B = 1$ for the AMPA-mediated component. The specific membrane resistance was set to 10,660 Ωcm^2 as in Hay et al.[75].

This process was repeated 50 times to obtain a range of EPSPs, each time with seven new synaptic contacts at random dendritic locations. Using the experimental trace of Bruno and Sakmann[7] as a target for fitting, our goal was to seek the synaptic conductance at each of the seven dendritic locations that yields a close match between model and experimental somatic EPSP. This resulted in maximal conductance of 0.31 nS per synaptic contact for both $\bar{g}_{AMPA}$ and $\bar{g}_{NMDA}$. We used the synaptic parameters found in this process for the TC synapses in our L2/3 pyramidal cell model, assuming that individual TC synaptic contacts have similar conductances in L4 and L2/3 pyramidal cells.

Equations (3)–(7) were also used to model CC synapses with a $\bar{g}_{AMPA}$ and $\bar{g}_{NMDA}$ conductance of 0.4 nS (as in Hay et al.[75]). The inhibitory synaptic conductance was modeled as for the AMPA conductance, with the following parameters, $E_{syn} = -80$ mv, $B = 1$, $\tau_{rise} = 0.18$ ms and $\tau_{decay} = 5$ ms[76].

Simulating visual input conveyed through thalamocortical synapses

For each model cell version, we placed TC, CC and inhibitory synapses as follows. The TC synapses were distributed randomly over the modeled dendritic tree such that, for each micrometer of dendritic length, the probability of having a TC synapse there is $1/TC_{density}$, where $TC_{density}$ is the measured synaptic density for the respective modeled cell. The same procedure was implemented for the CC synapses, based on their experimental density. Notably, the experimental excitatory synapse density that we consistently find in our studies[23,24,59] is much lower than reports for S1 (ref. [77]). This could be due to the different sensory modality or to differences in mouse strains. To compensate for 'missing' spines seen in MAP but not two-photon imaging, we added 20% to both cortical and thalamic synaptic densities based on the comparison between in vivo and MAP synapse counts. Inhibitory synapses were distributed randomly at 7.5-fold lower density than excitatory synapses (namely, their density was $(TC_{density} + CC_{density})/7.5$, as experimentally determined by Iascone et al.[77]).

To simulate visual input from the LGN to V1, we used sine waves at different frequencies with different contrast. The sine wave determined the instantaneous firing rate of the TC synapses. The average TC firing rate was set to be 2 Hz, and the maximum (that is, at 100% contrast) was 7.5 Hz[78]. The contrast was set between 0% and 100% similar to ref. [31]: when contrast was 0, the magnitude of the sine wave was 0, and the TC firing rate was 2 Hz. As the contrast increased, the magnitude

of the sine wave increased, until a maximum of 7.5 Hz at 100% contrast. When the sine wave determined the value of the firing rate to be lower than 0 Hz, it was truncated, such that the firing rate of the respective TC/CC synapses was always between 0 and 7.5 Hz. In our simulations, 88% of the background CC synapses fired randomly, with firing rates sampled from a Poisson process with $\lambda = 2$ Hz. The other 12% of CC synapses represent synapses arriving from L4 cells that are known to receive major thalamic inputs. The firing rate of these CC synapses was also modulated as was the rate of TC synapses. These CC modulated synapses were activated with delay of 5 ms with respect to the TC synapses, accounting for the additional (bi-synaptic) delay from L4-to-L2/3 pathway. The firing rate of inhibitory synapses was randomly sampled from a Poisson process with $\lambda = 5$ Hz.

Linear regression readout model

Our findings show a large variability in synaptic density (of both TC and CC synapses) among our nine experimental L2/3 cells. This suggests that a given visual input would generate a variable output response among different L2/3 cells. To what degree could one infer ('read out') the parameters of the visual input (for example, contrast) based on such a variable output? To answer this question, we utilized the detailed biophysical model of an L2/3 pyramidal cell (see above) receiving simulated visual input via its TC synapses (see above). Nine versions of this model (models 1–9) were constructed, each based on the density/number of the TC and CC synapses as measured from the respective experimental cell (Fig. 5). Each model received a 1-s-long simulated visual input of different contrasts and 4-Hz frequency, as described above, and the number of output spikes for each case were recorded. The visual contrast varied between 0% and 100%, with steps of 10%; each combination of cell and contrast was simulated for 100 repetitions (varying the dendritic location of TC and CC synapses but preserving their average density as in the respective experimental cell). This yielded 100 firing rates for each cell for each contrast. We then divided this dataset to 50 training examples and 50 test examples for each cell/contrast pair. For the individual neuron readout, we trained a linear regression model, $\hat{y} = a \times x + b$, where x is the firing rate of the cell, and $\hat{y}$ is the contrast. For the population readout, we trained the same linear regression model, but now x was a vector of firing rates from the nine cell models receiving visual inputs of a specific contrast. We used ordinary least squares to train the model and tested its performance on the test set[79]. The quality of the readout performance was assessed using Pearson correlation (R^2) between the prediction and ground truth (Fig. 6a).

We repeated the above computational experiment using only one cell model, which provided the best readout (cell 6; Fig. 6a). In this case, we simulated the cell's model for 1,000 repetitions (no statistical methods were used to predetermine sample sizes, but 1,000 repetitions were reported as sufficient in previous publications[77]), each with different random synaptic placements and synaptic activation time, and divided them into ten identical models with 100 repetitions each. We used these ten cells (all are identical to cell 6) to train a model to predict the visual contrast at 4-Hz input frequency. Next, to estimate the readout accuracy as a function of the number of cells used by the model, we fitted the data by the function $f(n) = a \times \log(n) + b$, where n is the number of cells and $f(n)$ is the readout accuracy of the model. To obtain the training data, we created nine separate linear regressors: one regressor using a single cell, one regressor using two cells, and so on, up to a regressor using all nine cells. This provided nine data points to extrapolate the readout accuracy of this model as a function of the number of cells used for the readout (Fig. 6d). Finally, to calculate the total average number of synapses used in each cell model, we summed the density of the TC and CC synapses, multiplied by the total length of the dendrites of the cell, and multiplied by 0.86 to account for the 50 μm proximal to the soma where we did not place excitatory synapses.

Reporting summary

Further information on research design is available in the Nature Portfolio Reporting Summary linked to this article.

Data availability

Data necessary to interpret, verify or extend the research in the article are available upon request.

Code availability

Synapses were annotated using ObjectJ, a freely available ImageJ plugin (https://sites.imagej.net/Kpberry/).

References

56. Vue, T. Y. et al. Sonic hedgehog signaling controls thalamic progenitor identity and nuclei specification in mice. *J. Neurosci.* **29**, 4484–4497 (2009).
57. Raymond, C. S. & Soriano, P. High-efficiency FLP and PhiC31 site-specific recombination in mammalian cells. *PLoS ONE* **2**, e162 (2007).
58. Tabata, H. & Nakajima, K. Efficient in utero gene transfer system to the developing mouse brain using electroporation: visualization of neuronal migration in the developing cortex. *Neuroscience* **103**, 865–872 (2001).
59. Chen, J. L. et al. Clustered dynamics of inhibitory synapses and dendritic spines in the adult neocortex. *Neuron* **74**, 361–373 (2012).
60. Lee, W. C. et al. A dynamic zone defines interneuron remodeling in the adult neocortex. *Proc. Natl Acad. Sci. USA* **105**, 19968–19973 (2008).
61. Kalatsky, V. A. & Stryker, M. P. New paradigm for optical imaging: temporally encoded maps of intrinsic signal. *Neuron* **38**, 529–545 (2003).
62. Schindelin, J. et al. Fiji: an open-source platform for biological-image analysis. *Nat. Methods* **9**, 676–682 (2012).
63. Ku, T. et al. Elasticizing tissues for reversible shape transformation and accelerated molecular labeling. *Nat. Methods* **17**, 609–613 (2020).
64. Dickstein, D. L. et al. Automatic dendritic spine quantification from confocal data with neurolucida 360. *Curr. Protoc. Neurosci.* **77**, 1.27.21–21.27.21 (2016).
65. Carnevale, N. T. & Hines, M. L. The NEURON Book (Cambridge University Press, 2006).
66. Segev, I. & Burke, R. E. in *Methods in Neuronal Modeling* (eds. C. Koch & I. Segev) (MIT Press, 1998).
67. Brent, R. P. Algorithms for minimization without derivatives (Courier Corporation, 2013).
68. Rapp, M., Yarom, Y. & Segev, I. The impact of parallel fiber background activity on the cable properties of cerebellar Purkinje cells. *Neural Comput.* **4**, 518–533 (1992).
69. Druckmann, S. et al. A novel multiple objective optimization framework for constraining conductance-based neuron models by experimental data. *Front Neurosci.* **1**, 7–18 (2007).
70. Markram, H. & et al Reconstruction and simulation of neocortical microcircuitry. *Cell* **163**, 456–492 (2015).
71. Spruston, N., Jonas, P. & Sakmann, B. Dendritic glutamate receptor channels in rat hippocampal CA3 and CA1 pyramidal neurons. *J. Physiol.* **482**, 325–352 (1995).
72. Rhodes, P. The properties and implications of NMDA spikes in neocortical pyramidal cells. *J. Neurosci.* **26**, 6704–6715 (2006).
73. Jahr, C. E. & Stevens, C. F. Voltage dependence of NMDA-activated macroscopic conductances predicted by single-channel kinetics. *J. Neurosci.* **10**, 3178–3182 (1990).
74. Doron, M., Chindemi, G., Muller, E., Markram, H. & Segev, I. Timed synaptic inhibition shapes NMDA spikes, influencing local dendritic processing and global I/O properties of cortical neurons. *Cell Rep.* **21**, 1550–1561 (2017).
75. Hay, E., Hill, S., Schurmann, F., Markram, H. & Segev, I. Models of neocortical layer 5b pyramidal cells capturing a wide range of dendritic and perisomatic active properties. *PLoS Comput. Biol.* **7**, e1002107 (2011).
76. Salin, P. A. & Prince, D. A. Spontaneous GABA$_A$ receptor-mediated inhibitory currents in adult rat somatosensory cortex. *J. Neurophysiol.* **75**, 1573–1588 (1996).
77. Iascone, D. M. et al. Whole-neuron synaptic mapping reveals spatially precise excitatory/inhibitory balance limiting dendritic and somatic spiking. *Neuron* **106**, 566–578 (2020).
78. Tang, J., Ardila Jimenez, S. C., Chakraborty, S. & Schultz, S. R. Visual receptive field properties of neurons in the mouse lateral geniculate nucleus. *PLoS ONE* **11**, e0146017 (2016).
79. Galton, F. Regression towards mediocrity in hereditary stature. *J. Anthropological Inst.* **15**, 246–263 (1886).

Author contributions

A.B. and E.N. designed the study. A.B. conducted all in vivo imaging experiments and data analysis. R.G. conducted all MAP experiments with T.K. and analyzed the data. R.G. developed two-photon scoring criteria based on MAP with A.B.'s help. T.K. established the MAP protocol under K.C.'s supervision. A.E. conducted all EM experiments and data analysis. K.B. contributed Extended Data Figs. 2 and 8. All modeling was done by M.D. with supervision by I.S. The manuscript was written by E.N. and I.S. with contributions from all authors.

Competing interests

The authors declare no competing interests.

Additional information

Extended data is available for this paper at https://doi.org/10.1038/s41593-022-01253-9.

Supplementary information The online version contains supplementary material available at https://doi.org/10.1038/s41593-022-01253-9.

Correspondence and requests for materials should be addressed to Elly Nedivi.

Peer review information *Nature Neuroscience* thanks the anonymous reviewers for their contribution to the peer review of this work.

Reprints and permissions information is available at www.nature.com/reprints.
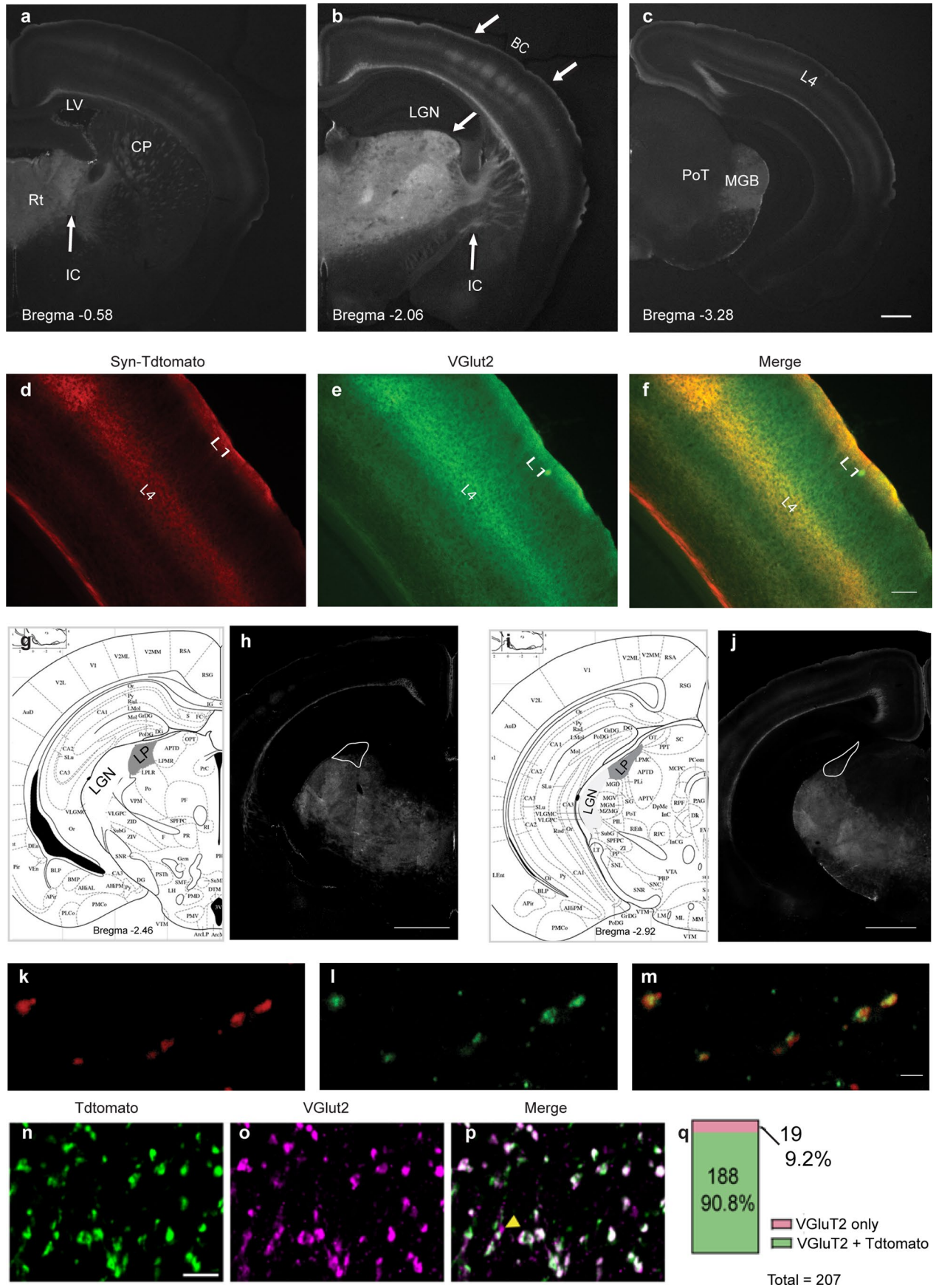
**Extended Data Fig. 1 | See next page for caption.**

Extended Data Fig. 1 | Crossing the Olig 3 Cre driver line to a Cre dependent Syn-Tdtomato reporter line faithfully and exclusively labels thalamic boutons from LGN but not LP. Olig3/+ mice were crossed with Ai14 reporter mice expressing Cre-dependent Tdtomato. **(a–c)** Sections at different Bregma coordinates on the anterior posterior axis of the brain show cellular labeling exclusive to thalamic nuclei, with thalamic afferents visible in the internal capsule and layer 4 of primary sensory cortices. **(d–f)** Sections through visual cortex immunostained for Tdtomato (red) and VGlut2 (green) show perfect overlap in thalamic afferents in layers 4 and 1. **g–j)** Coronal sections at Bregma coordinates that include both LP and LGN show predominantly LGN labeling in Olig3$^{-/+}$/Ai14 mice. Thal, thalamus; PoT, posterior thalamic nucleus; MGB, medial geniculate body; L4, cortical layer 4; L1, cortical layer1; BC, barrel cortex; LGN, lateral geniculate nucleus; IC, internal capsule; CP, caudate putamen; LV, lateral ventricle. **(k–m)** High magnification view in layer 2/3 of visual cortex showing beads-on-a-string appearance of thalamic boutons and specificity of VGlut2 staining to these boutons. **(n-p)** MAP processed sample labeled with **n)** anti-RFP to label genetically encoded tdTomato in thalamic boutons, and **o)** VGluT2. **p)** Composite image shows that all thalamic boutons genetically encoded with tdTomato, also are VGluT2 positive. **q)** Quantification of RFP and Vlut2 bouton co-labeling in MAP processed samples. Approximately 91% of Vglut2 boutons are RFP positive, with 9% potentially representing non-thalamic inputs. All (100%) RFP labeled boutons were Vlut2 positive. Brains from three animals were sectioned and imaged, and representative sections are shown in **a–f, h, j, k–p)**. Scale bars: (a-c) 0.5 mm; (d–f) 100 µm; (h–j) 1 mm; (k–m) 2 µm; (n-p) 10 µm.
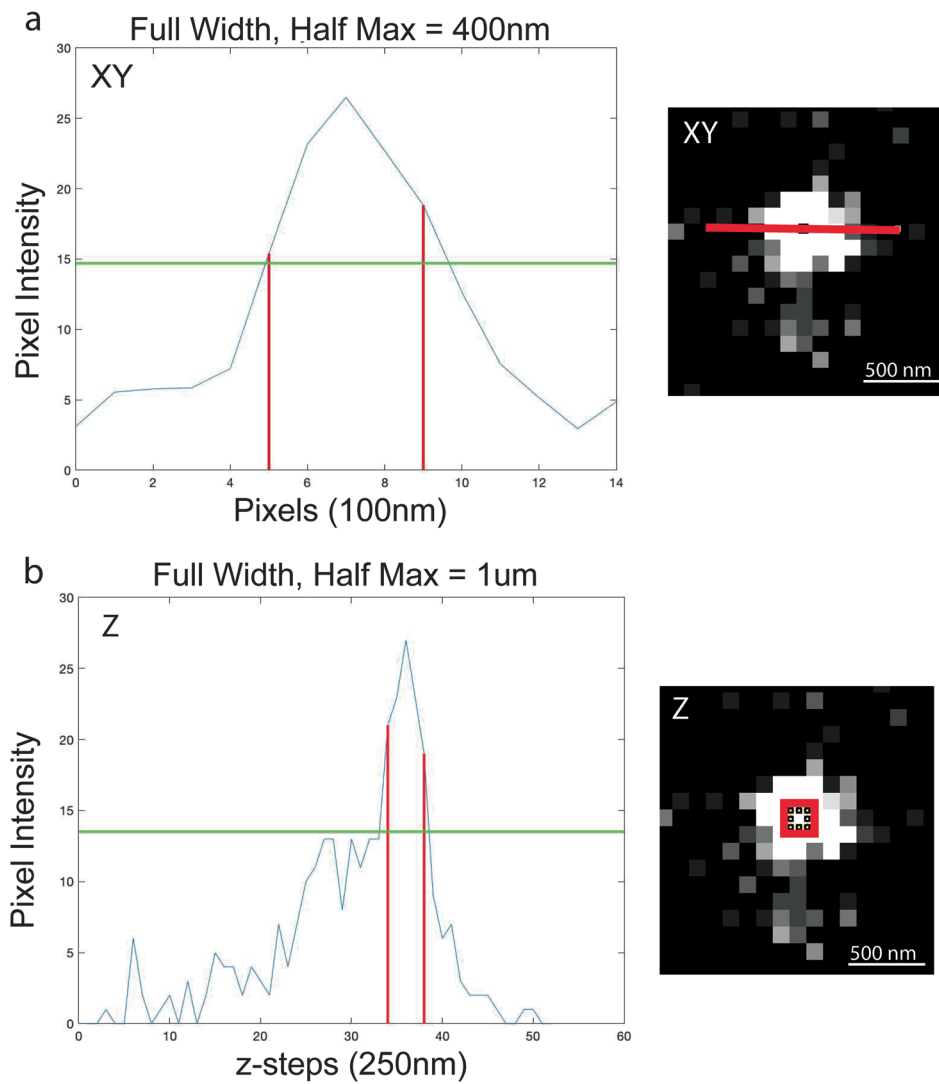
Extended Data Fig. 2 | Two photon imaging system alignment is compatible with its theoretical diffraction limited resolution. Two hundred nm fluorescent bead imaged on 2-photon system with a 1.0 NA objective at 915 nm with 100 nm/pixel XY sampling and 250 nm Z steps. **a)** Intensity plot on the XY axis (shown in red) with full width half maximum measured as 400 nm, as predicted by the Abbe limit. **b)** Intensity plot of the Z axis with full width half maximum measured as 1um.
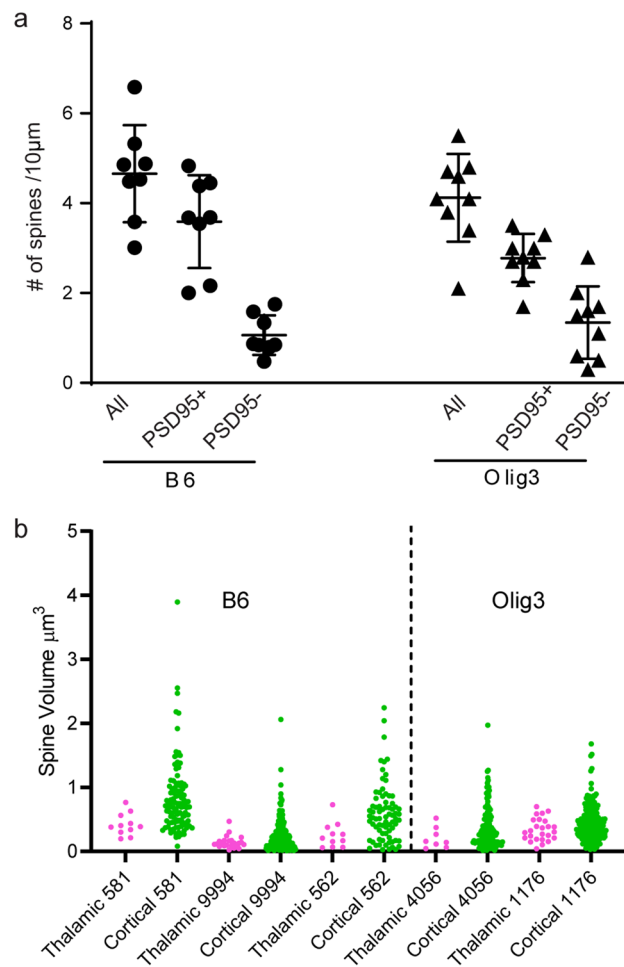
Extended Data Fig. 3 | Genetic background and plasmid system do not affect spine and synaptic densities, or spine volumes, on imaged neurons. a) To confirm that the Olig3/Syntd genetic background and use of the Flp/FRT vs Cre/lox plasmid system does not influence synaptic densities, densities of all, PSD95 + , and PSD95- spines were compared with previously published data[1]. No difference was found between backgrounds and plasmid systems in any category of spines imaged imaged (Nested t test, t(4)= 0.2585, p = 0.808, n = 51 from 17 animals). **b)** Thalamic vs cortical dendritic spine volumes were compared in MAP images of L2/3 labeled neurons from B6 vs Olig3 mice, where thalamic synapses were identified by VGlut2 staining. Scatter plots of spine sizes shown per each MAP cell demonstrate that synaptophysin expression does not influence either thalamic (Nested t test, t(3) = 0.07544, p = 0.9446, n = 78 spines from 5 animals) or cortical dendritic spine volumes (Nested t test, t(3) = 0.6727, p = 0.5493, n = 721 spines from 5 animals).
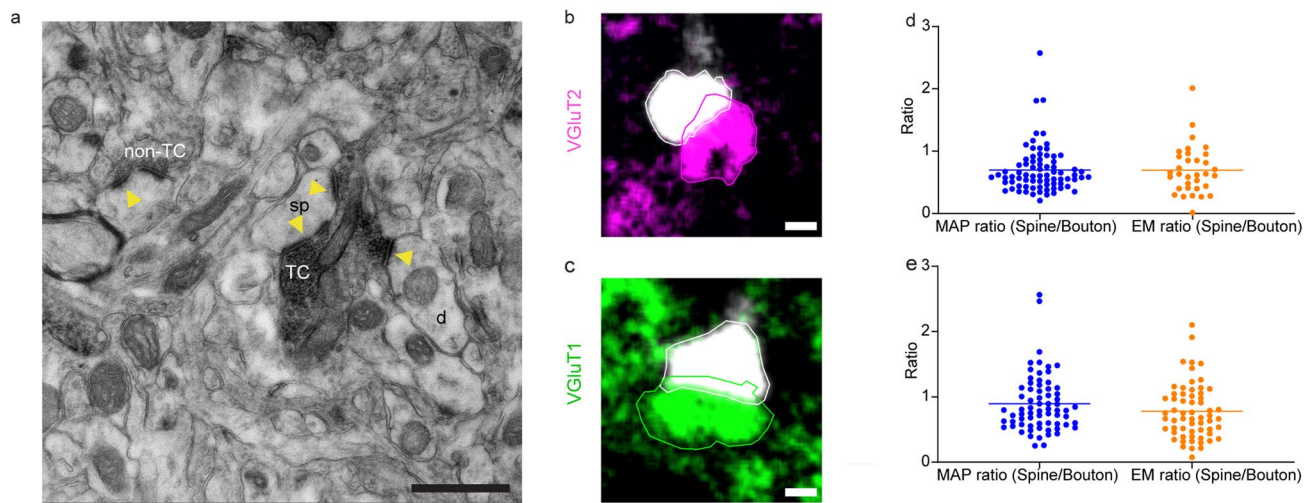
Extended Data Fig. 4 | Comparison of EM and MAP validates that MAP expands tissue uniformly. a) Representative EM image showing a VGluT2+ terminal bouton (TC) that forms a perforated synapse on a spine (sp), and a small, non-perforated synapse on a dendrite shaft (d; identified by the presence of a mitochondria within). Yellow arrowheads mark synaptic zones from the postsynaptic side. An unlabeled terminal bouton (non-TC) that forms a perforated synapse on a spine is also marked. Scale bar = 250 nm. **b)** Magnification of 1 x-y plane of a MAP imaged dendritic spine, shown in white, with Vglut2 labeled terminal bouton (thalamic, magenta). Contours for measurement of spine area and terminal bouton area are shown. **c)** Same as b) but with a spine contacting a VGluT1 labeled bouton (cortical, green). Scale bars = 1 µm. **d)** Ratio of spine head area/terminal bouton area match for MAP and EM for thalamic synapses (Mann–Whitney U test, p = 0.9399, n = 76 for MAP and 33 for EM) and **e)** cortical synapses (Mann–Whitney U test, p = 0.1056, n = 69 for MAP and 61 for EM). Sp, dendritic spine; D, dendrite.
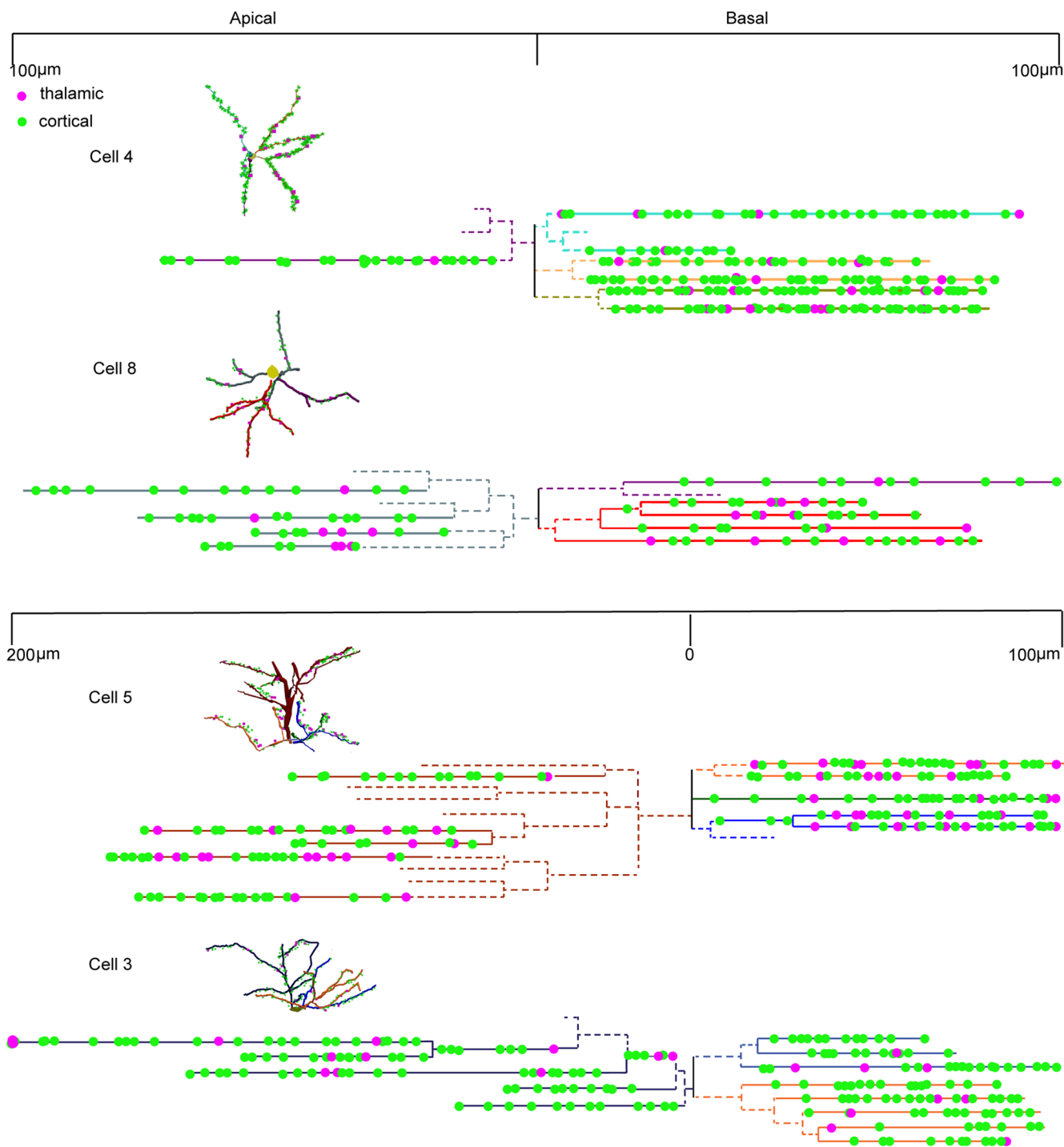
Extended Data Fig. 5 | Distribution of thalamic vs cortical inputs onto L2/3 neurons. Additional dendrograms showing the distribution of thalamic versus cortical inputs onto the dendritic arbors of four additional pyramidal neurons in L2/3 of binocular V1 not presented in Fig. 4. Apical and basal dendrites are shown on opposite sides of the cell body (marked as 0 on the scale). The scale illustrates the distance of each input from the cell body. Note that cells 5 & 3, are deeper, and shown on a different scale. Dashed lines depict branch segments that were traced, but not scored. Insets (top left) in each dendrogram show the traced skeleton of that cell with location of scored inputs.
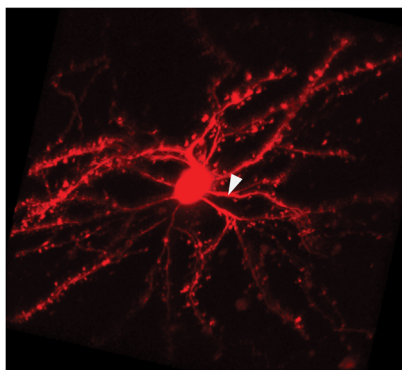
Soma: 89um
Branch: 15
Length: 1004um
Tdensity: 0.2 /10um
Cdensity: 2 /10um
Thalamic: 8%
Cortical: 92%
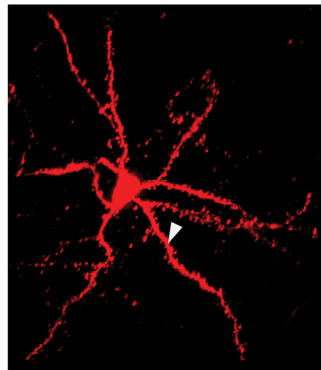
Soma: 144um
Branch: 7
Length: 699um
Tdensity: 0.3 /10um
Cdensity: 3 /10um
Thalamic: 8%
Cortical: 92%
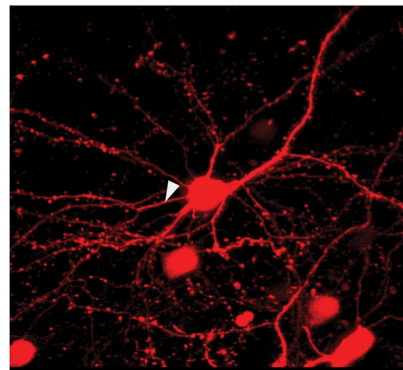
Soma: 163um
Branch: 17
Length: 1125um
Tdensity: 0.5 /10um
Cdensity: 3 /10um
Thalamic: 13%
Cortical: 87%
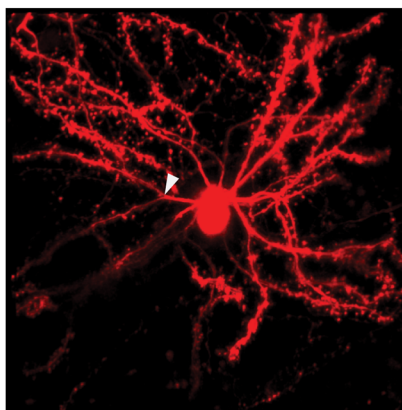
Soma: 96um
Branch: 15
Length: 1445um
Tdensity: 0.3 /10um
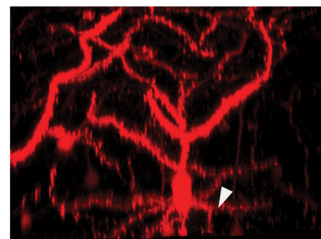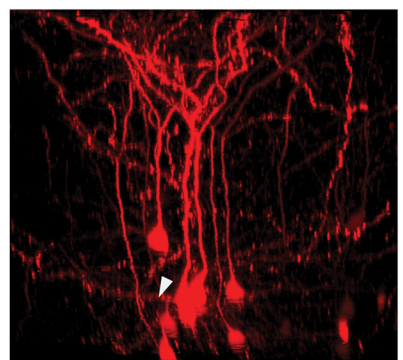Cdensity: 2.7 /10um
Thalamic: 13%
Cortical: 87%
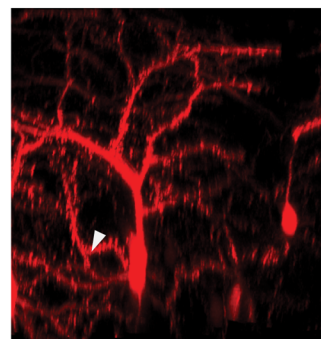
Soma: 153um
Branch: 10
Length: 743um
Tdensity: 0.7 /10um
Cdensity: 2.2 /10um
Thalamic: 19%
Cortical: 81%
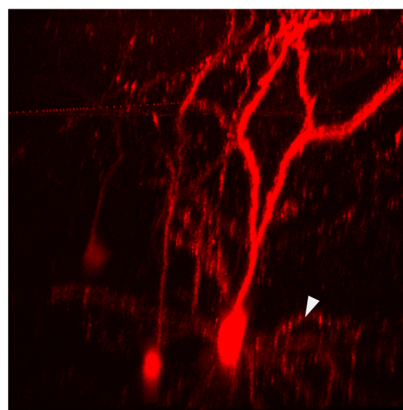
Soma: 188um
Branch: 9
Length: 616um
Tdensity: 0.3 /10um
Cdensity: 1.4 /10um
Thalamic: 19%
Cortical: 81%
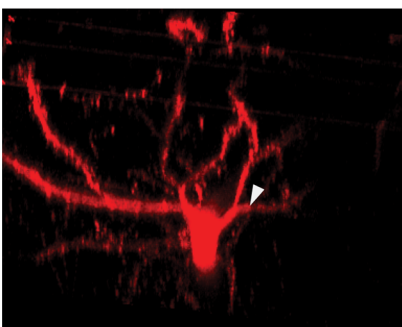
Soma: 121
Branch: 14
Length: 1084um
Tdensity: 0.2 /10um
Cdensity: 1.7 /10um
Thalamic: 8%
Cortical: 92%

Soma: 159um
Branch: 11
Length: 1090um
Tdensity: 0.5 /10um
Cdensity: 2.5 /10um
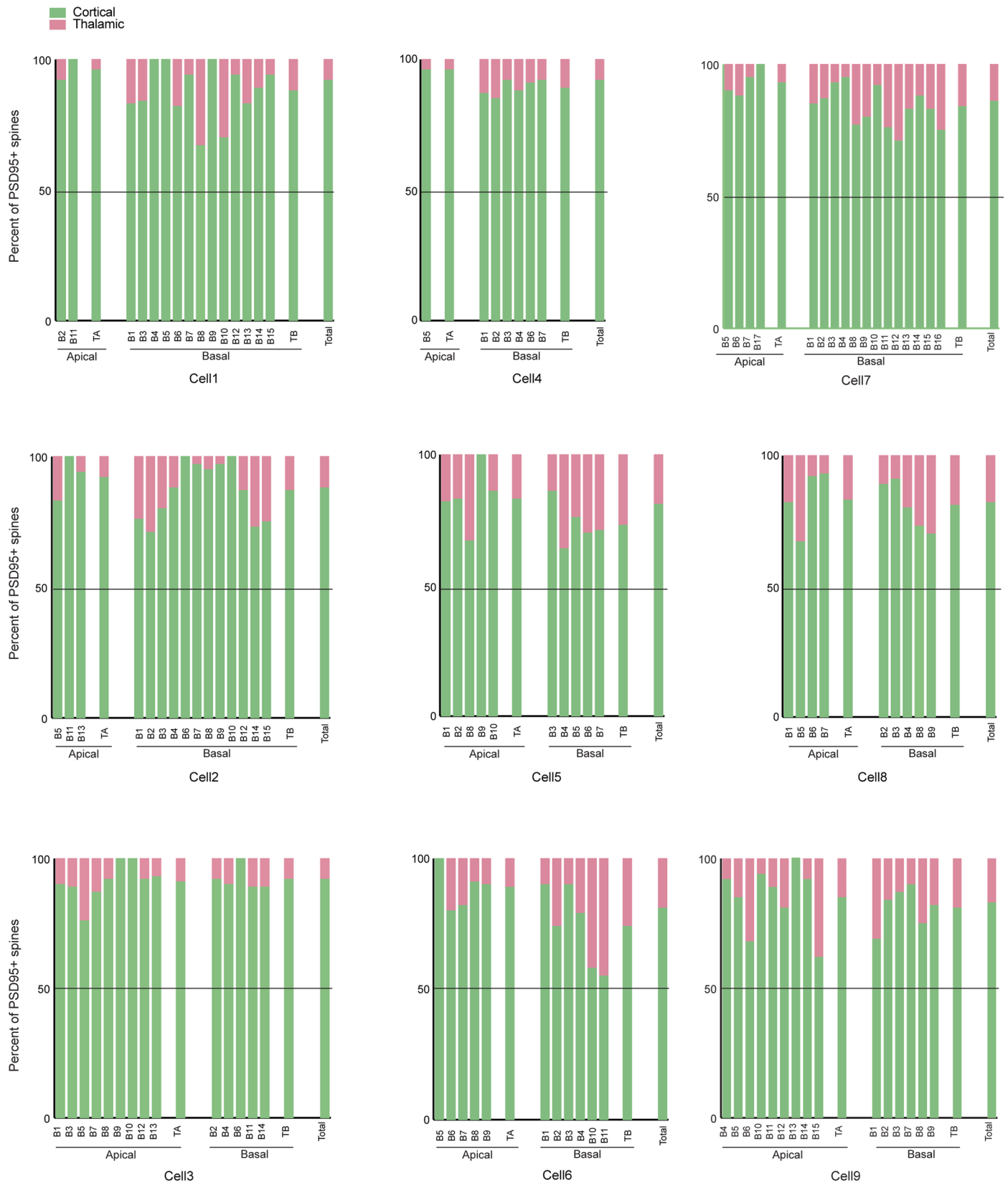Thalamic: 21%
Cortical: 79%

Soma: 208um
Branch: 15
Length: 1125um
Tdensity: 0.4 /10um
Cdensity: 2 /10um
Thalamic: 12%
Cortical: 88%

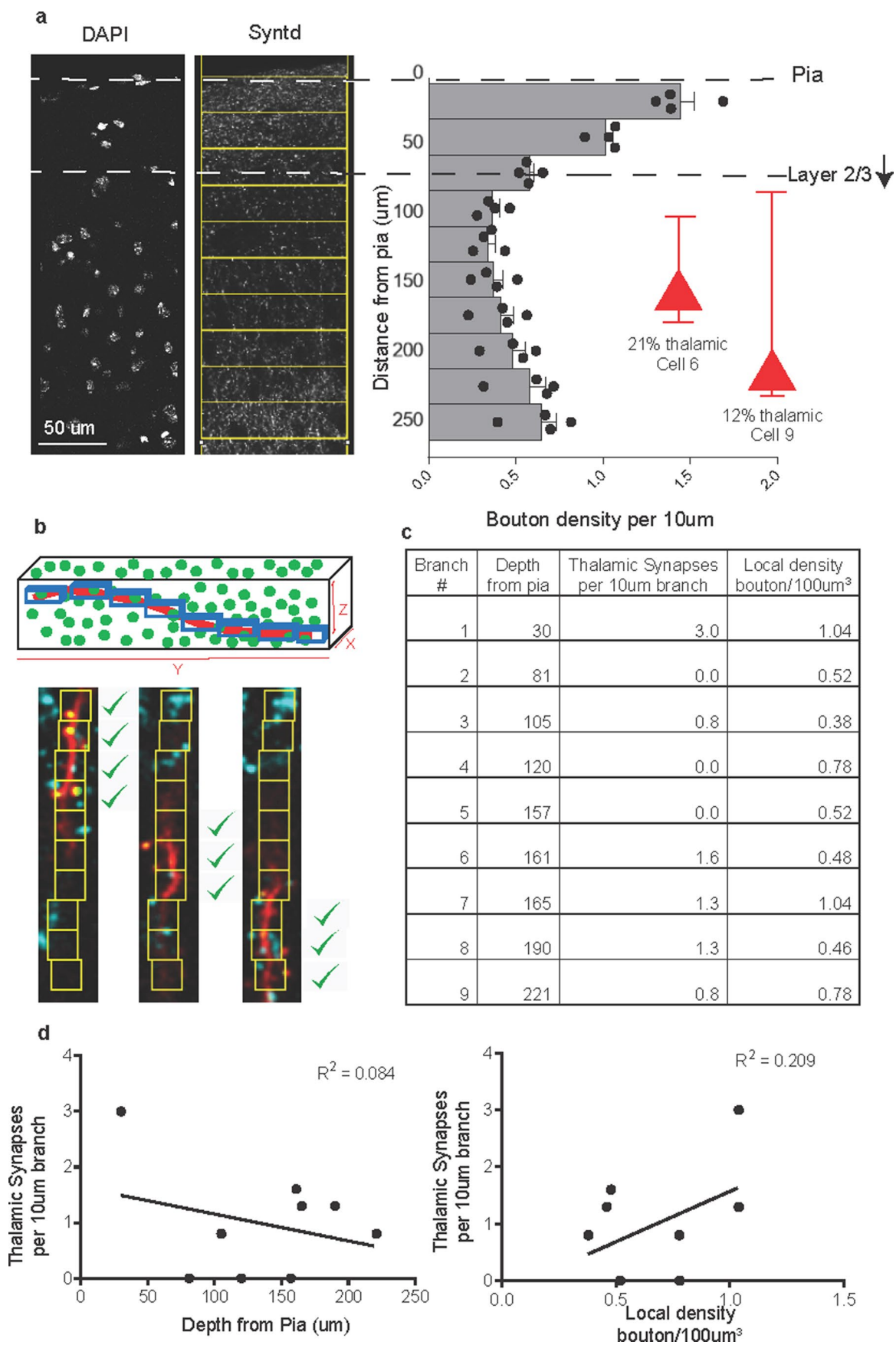**Extended Data Fig. 6 | See next page for caption.**

Extended Data Fig. 6 | Diverse morphology and statistics of the nine pyramidal cells analyzed. Maximum intensity projections of cells imaged *in vivo* are presented in order of somal depth in relation to pia, with top left most superficial and bottom right deepest. Note that superficial cells have atypical apical dendrites as compared to deeper cells. They also tend towards more extensive basal dendrites (for example, Cell 1 has 13 basal dendrites while having only 2 apical dendrites. A similar morphology exists for Cell 2), while deeper cells have more apical and fewer basal dendrites (for example, Cell 9). Since distinction of basal vs apical is not always obvious in the maximum intensity projections, white arrows point to a basal dendrite for each cell, and an appended movie file shows a representative Z stack. A representative Supplementary video 1 shows a Z stack of Cell 7 encompassing both apical and basal dendrites. See Fig. 4c–d in main text for number of apical vs basal dendrites scored for each cell.

Extended Data Fig. 7 | Thalamic inputs are heterogeneously distributed across individual branches of pyramidal cells, and across cells. The overall percent of the thalamic vs. cortical synapses onto individual branches (marked as B followed by branch number) of all nine pyramidal cells imaged, with apical branches on the right and basal dendrites on the left for each cell. TA, TB, and Total summarize total apical and total basal, and total per cell, respectively.

a

DAPI   Syntd

b

c

Branch #	Depth from pia	Thalamic Synapses per 10um branch	Local density bouton/100um³
1	30	3.0	1.04
2	81	0.0	0.52
3	105	0.8	0.38
4	120	0.0	0.78
5	157	0.0	0.52
6	161	1.6	0.48
7	165	1.3	1.04
8	190	1.3	0.46
9	221	0.8	0.78

d

Extended Data Fig. 8 | See next page for caption.

Extended Data Fig. 8 | Thalamic innervation is not correlated with dendritic branch depth or local bouton density. a) Coronal section through visual cortex stained with DAPI (left) from Olig3/synTd mouse showing synTd labeling of thalamic pre-synaptic boutons (middle). SynTd boutons were counted per 100x25um bins and their density was plotted as a function of distance from the pial surface (right). Error bars: SEM n = 4 mice. Red triangles are a schematic representation of Cell 6 and Cell 9 with their respective % thalamic innervation. Their somal depth with basal and apical dendrite span are mapped in relation to the bouton density graph. While both Cell 6 & 9 are within L2/3, because of their different somal depth, their basal dendrites extend to to different depths. Although Cell 9 basal dendrites project much deeper than those of Cell 6 into a region with higher thalamic bouton density, Cell 6 has almost double the thalamic innervation. **b)** Diagram demonstrating how thalamic innervation onto specific dendritic branches was scored in relation to local thalamic bouton density, with 4x4um ROIs placed around each branch segment imaged *in-vivo* in the z-planes where it was brightest (green: synTd, cyan: PSD95-teal, red: YFP). **c)** Representative branches varying in depth were scored as shown in **b**, showing the number of thalamic synapses on each branch is unrelated branch depth or local thalamic bouton density. **d)** Linear regression comparing density of thalamic synapses on branches versus depth from pia (left) and local bouton density (right), including data from **c**, shows no correlation between branch depth, local thalamic bouton density, and number of thalamic contacts per branch.; $r^2 = 0.084$ p = 0.449 and $r^2 = 0.209$ p = 0.215 respectively.
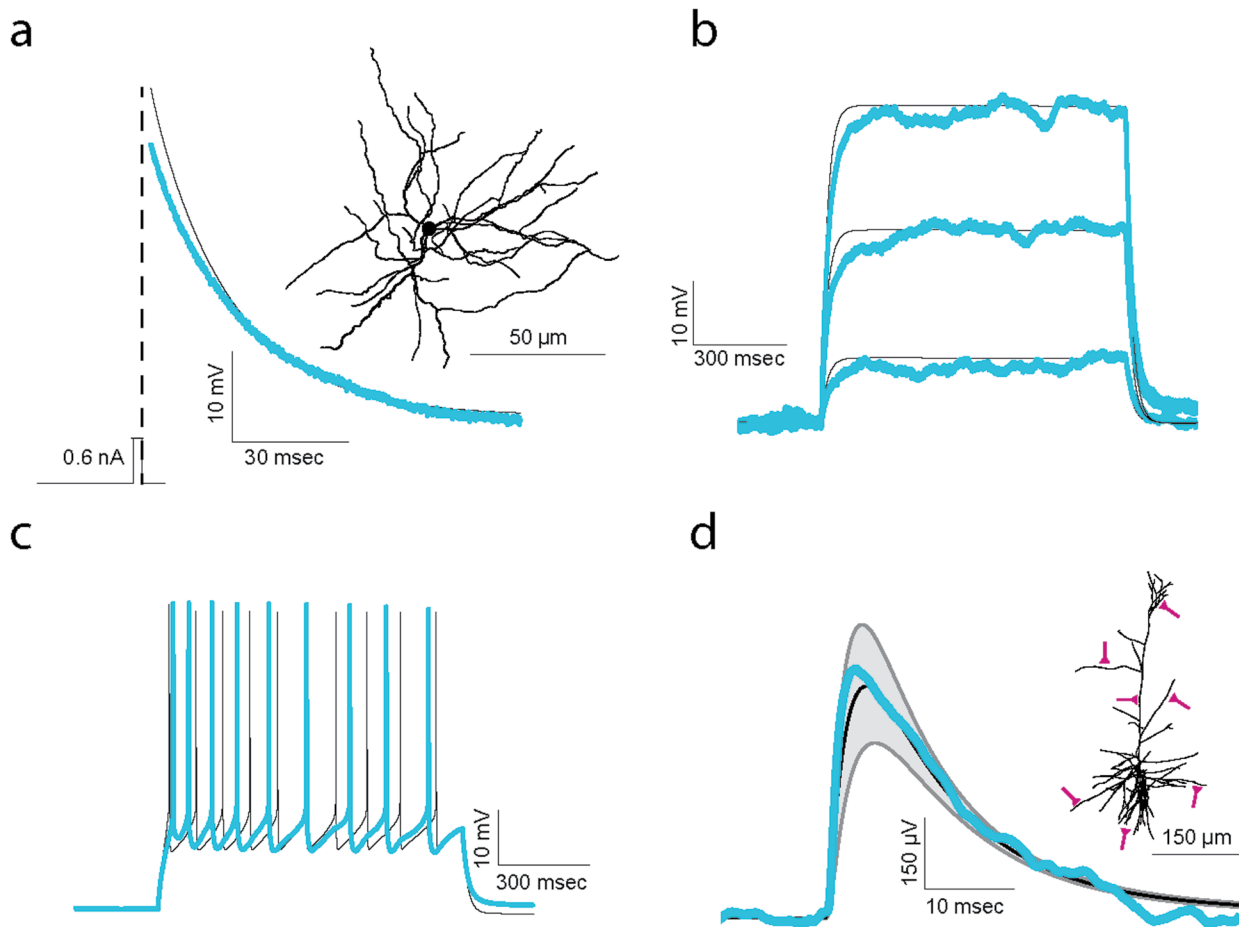
Extended Data Fig. 9 | Experimentally based model of L2/3 pyramidal cell in V1. (a) Voltage response of typical cell (shown in inset) following a 3 msec and 0.6 nA subthreshold depolarizing step current. Blue, experimental trace; black, model. The morphology and physiology of this cell was taken from the Allen Institute Cell Atlas (see Methods). **(b)** Voltage response of the cell shown in **a** to three subthreshold long current pulses (0.01 nA, 0.03 nA and 0.05 nA, given for 1000 msecs). Blue, experimental trace; black, model. **(c)** Spiking response of the cell shown in **a** (in blue) to suprathreshold current injections (1.17 nA for 1000 msecs); model response is shown in black. **(d)** The response of a L4 cortical pyramidal cells model (inset, cell reconstructed by the Blue Brain Project, see

Methods) to the activation of a single thalamo-cortical axon. The experimental somatic EPSP is shown in blue (courtesy of Randy Bruno, see Methods); thick black line shows the average EPSP in the biophysical model constructed for this L4 cell in response to the simultaneous activation of 7 synaptic contacts (red synapses). The gray area shows the standard deviation around the mean of the somatic EPSPs in repeated activation of 7 synaptic contacts that were randomly distributed repeatedly across the modelled dendritic tree. The best fit was achieved with peak conductance of 0.31 nS for both the AMPA- and the NMDA- components; see Methods for details of synapse and neuron models.

nature research

Corresponding author(s): Elly Nedivi

Last updated by author(s): 2022 11 03

Reporting Summary

Nature Research wishes to improve the reproducibility of the work that we publish. This form provides structure for consistency and transparency in reporting. For further information on Nature Research policies, see our Editorial Policies and the Editorial Policy Checklist.

Statistics

For all statistical analyses, confirm that the following items are present in the figure legend, table legend, main text, or Methods section.

n/a	Confirmed	
☐	☒	The exact sample size (*n*) for each experimental group/condition, given as a discrete number and unit of measurement
☐	☒	A statement on whether measurements were taken from distinct samples or whether the same sample was measured repeatedly
☐	☒	The statistical test(s) used AND whether they are one- or two-sided *Only common tests should be described solely by name; describe more complex techniques in the Methods section.*
☐	☒	A description of all covariates tested
☐	☒	A description of any assumptions or corrections, such as tests of normality and adjustment for multiple comparisons
☐	☒	A full description of the statistical parameters including central tendency (e.g. means) or other basic estimates (e.g. regression coefficient) AND variation (e.g. standard deviation) or associated estimates of uncertainty (e.g. confidence intervals)
☐	☒	For null hypothesis testing, the test statistic (e.g. *F*, *t*, *r*) with confidence intervals, effect sizes, degrees of freedom and *P* value noted *Give P values as exact values whenever suitable.*
☒	☐	For Bayesian analysis, information on the choice of priors and Markov chain Monte Carlo settings
☒	☐	For hierarchical and complex designs, identification of the appropriate level for tests and full reporting of outcomes
☐	☒	Estimates of effect sizes (e.g. Cohen's *d*, Pearson's *r*), indicating how they were calculated

Our web collection on statistics for biologists contains articles on many of the points above.

Software and code

Policy information about availability of computer code

Data collection	Microscope instrumentation was controlled using LabView (National Instruments; Austin, Texas) version 17.0
Data analysis	python 3.7.6, NEURON 7.7.2, Adobe Illustrator 2021, Fiji ImageJ 1.52p, Object J Version 3, Matlab 2017b, Graphpad Prism 6, Neurolucida 360 2.70.6

For manuscripts utilizing custom algorithms or software that are central to the research but not yet described in published literature, software must be made available to editors and reviewers. We strongly encourage code deposition in a community repository (e.g. GitHub). See the Nature Research guidelines for submitting code & software for further information.

Data

Policy information about availability of data

All manuscripts must include a data availability statement. This statement should provide the following information, where applicable:
- Accession codes, unique identifiers, or web links for publicly available datasets
- A list of figures that have associated raw data
- A description of any restrictions on data availability

Data availability statement provided: Data necessary to interpret, verify, or extend the research in the article is available upon request.

Field-specific reporting

Please select the one below that is the best fit for your research. If you are not sure, read the appropriate sections before making your selection.

☒ Life sciences   ☐ Behavioural & social sciences   ☐ Ecological, evolutionary & environmental sciences

For a reference copy of the document with all sections, see nature.com/documents/nr-reporting-summary-flat.pdf

Life sciences study design

All studies must disclose on these points even when the disclosure is negative.

Sample size	Methods now have a separate Data Analysis, Statistics and Reproducibility for each experimental protocol, where sample size selection is discussed
Data exclusions	No data exclusion
Replication	Each Figure legend now includes number of replications
Randomization	All data was essentially one experimental group.
Blinding	Methods now have a separate Data Analysis, Statistics and Reproducibility for each experimental protocol, where blinding is discussed as appropriate

Reporting for specific materials, systems and methods

We require information from authors about some types of materials, experimental systems and methods used in many studies. Here, indicate whether each material, system or method listed is relevant to your study. If you are not sure if a list item applies to your research, read the appropriate section before selecting a response.

Materials & experimental systems

n/a	Involved in the study
☐ ☒	Antibodies
☒ ☐	Eukaryotic cell lines
☒ ☐	Palaeontology and archaeology
☐ ☒	Animals and other organisms
☒ ☐	Human research participants
☒ ☐	Clinical data
☒ ☐	Dual use research of concern

Methods

n/a	Involved in the study
☒ ☐	ChIP-seq
☒ ☐	Flow cytometry
☒ ☐	MRI-based neuroimaging

Antibodies

Antibodies used	Described in methods section and Supp. Table 3.
Validation	RRITs provided in Supp.Table 3

Animals and other organisms

Policy information about studies involving animals; ARRIVE guidelines recommended for reporting animal research

Laboratory animals	C57/BL6 mice, Olig3-Cre mice, SynTD reporter mice (Jackson # 012570), Ai14 reporter mice (Jackson # 007914); two months old; male and female. Mice were housed in standard static caging with hardwood bedding with 12/12 lighting, 7am sunrise and 7pm sunset, and room temperature maintained at 70 degrees F +/- 2 degrees and 30 -70% humidity.
Wild animals	no wild animals were used in this study
Field-collected samples	no field-collected samples were used in this study
Ethics oversight	All animal procedures were approved by the Institutional Animal Care and Use Committees at the Massachusetts Institute of Technology and University of Virginia, and meet the NIH guidelines for the use and care of vertebrate animals.

Note that full information on the approval of the study protocol must also be provided in the manuscript.